Journal of Science: Advanced Materials and Devices 10 (2025) 100974

Contents lists available at ScienceDirect

Journal of Science: Advanced Materials and Devices

journal homepage: www.elsevier.com/locate/jsamd

Research Article

Tailoring porosity and antibacterial activity in MgO/ZrO_2-modified kaolin ceramics for use in wastewater filtration systems

Dikra Bouras [a], Mamoun Fellah [c,d,*], Billel Salhi [b,**], Nestor Ankah [e], Neçar Merah [e,f]

[a] Department of Science of Matter, Faculty of Science and Technology, University of Souk-Ahras, Algeria
[b] Interdisciplinary Research Center for Membranes and Water Security, King Fahd University of Petroleum and Minerals, Dhahran, 31261, Saudi Arabia
[c] Mechanical Engineering Department, ABBES Laghrour- University Khenchela, PO 1252, CP, 40004, Algeria
[d] Biomaterial, Synthesis and Tribology Research Team, Khenchela University, 40004, Algeria
[e] Interdisciplinary Research Center for Advanced Materials, King Fahd University of Petroleum and Minerals, 31261, Dhahran, Saudi Arabia
[f] Mechanical Engineering Department, King Fahd University of Petroleum and Minerals, Box 1180, Dhahran, 31261, Saudi Arabia

ARTICLE INFO

Keywords:
DD2Z+80 wt%MgO
Kaolinite ceramics
Antibacterial activity
Water purification

ABSTRACT

The advancement of natural ceramic materials with multifunctional properties is essential for promoting sustainable solutions in wastewater treatment and microbial control. This study examines kaolinite-based ceramics from Algerian DjebelDebbagh clay (DD2) modified with magnesium oxide (MgO) at concentrations of 0, 40, and 80 wt%, both with and without the addition of 38 wt% zirconium dioxide (ZrO_2) (DD2Z), to evaluate their structural, adsorptive, and antibacterial properties. Ceramic composites were synthesized through high-temperature sintering and characterized using X-ray diffraction (XRD), scanning electron microscopy with energy-dispersive X-ray spectroscopy (SEM/EDS), Brunauer-Emmett-Teller (BET) surface area analysis, thermogravimetric analysis (TGA) and atomic force microscopy analysis (AFM). Phase analysis indicated the development of mullite, spinel, zircon, and magnesium silicate phases, which progressed with higher MgO content. The incorporation of ZrO_2 enhanced mesoporosity and surface area, whereas MgO improved permeability and facilitated bacterial inactivation. The antibacterial activity against Pseudomonas putida was assessed through immersion and agar diffusion methods, revealing that the DD2Z + 80 wt% MgO sample demonstrated the highest inhibition rate of 75 % and the largest inhibition zone measuring 12.5 mm. Liquid diffusion tests confirmed enhanced wettability and pore connectivity in the ZrO_2-MgO systems. The findings indicate that MgO- and ZrO_2-modified natural kaolinite ceramics may serve as cost-effective, durable, and antibacterial materials suitable for integrated wastewater treatment applications.

1. Introduction

Microbes are incredibly diverse and among the most widespread life forms on Earth. Recent work by Guo et al. [1] has documented alarming antibiotic resistance patterns in urban wastewater systems, highlighting the urgent need for advanced treatment solutions. They are capable of surviving in some of the harshest environments, including extremely hot or cold climates, acidic or radioactive zones, high-pressure locations, and areas with high salinity [2,3]. These microorganisms exist in the air, soil, water, and even inside the human body and food, where they can be responsible for numerous infections affecting people, animals, and plants [4,5]. Ongoing research has revealed a troubling trend: the continued use of antibiotics has led to the rise of resistant bacterial strains. This aligns with findings by Li et al. [6], who demonstrated how conventional biochar treatments become ineffective against metal-resistant bacteria in complex wastewater matrices, contributing to illnesses with increasingly high mortality rates [7,8].

Researchers selected three bacterial species for testing: two Gram-positive strains (*Staphylococcus aureus*, *Bacillus subtilis*) and one Gram-negative strain (*Pseudomonas putida*), chosen for their environmental relevance and resistance characteristics. *Staphylococcusaureus* (*S. aureus*) is a toxin-producing bacterium commonly found in human nasal passages and food sources [9–15]. *Bacillussubtilis* (*B. subtilis*) is a spore-forming soil microorganism with high resistance to stress conditions [16–18]. *Pseudomonasputida* (*P.putida*) is widespread in natural and clinical environments and shows strong resistance to antimicrobials,

* Corresponding author. Biomaterial, Synthesis and Tribology Research Team, Khenchela University, 40004, Algeria.
** Corresponding author.
E-mail addresses: mamoune.fellah@univ-khenchela.dz (M. Fellah), billel@kfupm.edu.sa (B. Salhi).

https://doi.org/10.1016/j.jsamd.2025.100974
Received 15 May 2025; Received in revised form 8 August 2025; Accepted 10 August 2025
Available online 14 August 2025

posing risks in post-surgical infections [19–23].

The rise of multidrug-resistant bacteria and the environmental persistence of synthetic pollutants demand urgent solutions that are both effective and economically viable [24]. Traditional disinfection methods and wastewater treatment approaches often fall short due to high operational costs, limited durability, and environmental concerns [25,26]. This study addresses the need for environmently friendly, multifunctional ceramic materials capable of simultaneous microbial control and pollutant removal [27–29].

Kaolinite from DjebelDebbagh (DD2) was chosen for its high purity (SiO_2: 45.29 wt%, Al_2O_3: 38.36 wt%) and thermal stability, making it suitable for ceramic applications [30,31]. Magnesium oxide (MgO) was added for its proven antibacterial activity via reactive oxygen species (ROS) generation and its role in forming spinel structures that enhance mechanical strength [32,33]. MgO also brings thermal stability, a wide band gap (Eg = 7.2 eV), and catalytic efficiency, making it ideal for combined antibacterial and filtration functions [34–36]. Zirconium dioxide was introduced at 38 wt%, to improve porosity (~33 %) and structural integrity during sintering, outperforming other oxides like TiO_2 under similar conditions [34,35]. Both MgO and ZrO_2 are widely used in water treatment and environmental remediation due to their stability and effectiveness [37–42]. Recent studies by Dai et al. [43] and Xu et al. [44] have demonstrated how oxide stabilization mechanisms in cementitious and ceramic systems can be adapted for wastewater applications. Their work with glass-modified cements and aluminum oxynitrides confirms that careful control of oxide interfaces enhances both structural stability and functional performance - principles we apply here through our MgO-ZrO_2-kaolinite composite design. Previous studies have also considered the removal of persistent dyes such as Methylene Blue and Orange II, which are toxic and non-biodegradable [45–47]. Conventional treatment methods often fail to fully eliminate such pollutants, while ceramic membranes provide better durability, selectivity, and energy efficiency [48,49].

While polymeric membranes dominate the commercial sector, ceramic membranes are gaining interest for their superior thermal and chemical resistance, mechanical stability, and longevity [50,51]. With advancements in nanotechnology, new antibacterial surfaces made from inorganic compounds have been developed. One such method is thermal autoclaving, which applies heat and pressure to reduce particle size and improve structural features [52,53]. Tuning the physical properties of these agents, such as size and surface structure, can significantly improve their antibacterial capabilities [54].

Beyond antibacterial properties, the developed ceramics show promise for integrated wastewater treatment systems [55]. Preliminary adsorption tests with methylene blue (50 mg/L solution) revealed 92 % removal efficiency within 120 min for DD2Z+40 wt% MgO, comparable to activated carbon benchmarks. This dual functionality stems from: (1) the mesoporous structure (2–50 nm pores) providing high surface area (16.31 m^2/g) for contaminant adsorption, and (2) the continuous antibacterial action preventing biofilm foulinga major limitation of conventional adsorbents. When configured as a membrane (0.5 mm thickness, 35 % porosity), the material demonstrated stable water flux of 120 L/m^2h at 0.5 bar pressure, suggesting practical viability for continuous flow systems.

For the first time, this study investigates the combined use of MgO and ZrO_2 in kaolinite-based ceramic composites for antibacterial and water treatment applications. Using DD2 kaolin as the base material, composites were synthesized with 0, 40, and 80 wt% MgO and a fixed 38 wt% ZrO_2. These ceramics were formed into pellets via sintering and characterized using Scanning Electron Microscopy (SEM), (EDS), (XRD), (BET), and (TGA). The functional performance was assessed through liquid diffusion tests and antibacterial evaluations, including immersion and agar diffusion methods against *Pseudomonas putida*.

The present approach differs from previous studies that typically focus on either antibacterial or adsorptive properties in isolation. By combining MgO and ZrO_2 within a sintered kaolinite matrix, a single ceramic material was designed to offer both high filtration performance and effective bacterial inhibition without the need for surface modification, chemical coatings, or polymer supports. The choice of environmentlly friendly natural Algerian kaolin and straightforward processing methods also improves scalability and cost-efficiency, which remain major limitations in current ceramic membrane development. The results provide valuable insights into how the structural and surface modifications brought by MgO and ZrO_2 enhance the multifunctionality of kaolinite-based ceramics. This work contributes to the development of durable, antibacterial ceramic membranes capable of efficient water purification and resistance to microbial contamination.

2. Materials and methods

2.1. Materials

The ceramic samples were developed using six compositions, as outlined in Table 1. The base material, kaolin from DjebelDebbagh (DD2), was obtained from a deposit located west of Guelma, Algeria (36°31′52″N, 7°16′03″E). This clay was selected for its known purity and suitability for high-temperature ceramic applications. To tailor the ceramic structure and improve functional performance, magnesium oxide (MgO) was added in two different weight percentages (40, and 80 wt%). Zirconium oxide (ZrO_2) was also incorporated at a constant 38 wt % to improve mechanical stability and enhance the pore structure. The chemical composition and purity of all materials used are summarized in Table 2.

2.1.1. Samples synthesis

The preparation began with raw kaolin (DD2) collected in block form. These blocks were first crushed mechanically, then screened to obtain a uniform grain size of 250 μm [56]. After screening, two batches of powder were prepared: one consisting of DD2 alone, and another in which 38 wt% zirconium oxide (ZrO_2) was added to the DD2 powder to improve thermal and mechanical properties [53,54]. This combination was done prior to any wet processing.

Both powder types underwent wet milling at 500 rpm for 20 min to ensure homogeneity and even particle distribution [57]. After milling, the slurries were dried, then calcined at 520 °C for 30 min to eliminate moisture, organic matter, and volatile impurities critical for thermal stability and proper phase formation [56,58]. The calcined powders were then blended with magnesium oxide (MgO) in three concentrations (0, 40, and 80 wt%) to modify the ceramic structure and further enhance functional properties [31,32].

To prevent agglomeration and ensure even distribution of ZrO_2 and MgO particles throughout the matrix, each composition was subjected to additional wet milling step (500 rpm, 20 min) using distilled water as the medium, followed by drying at 105 °C. This repeated dispersion process helped break up soft agglomerates and improved interparticle contact.

These mixtures were thoroughly homogenized, molded into discs using uniaxial pressing at 0.9 tons for uniform compaction [56,58], and subjected to sintering at 1300 °C (5 °C/min heating rate, 2 h dwell) to initiate phase consolidation. A final high-temperature treatment at 1400 °C under the same heating conditions promoted full densification and phase development. Each step in this sequence is reflected precisely in the updated Fig. 1 to align with the experimental flow and ensure reproducibility.

Table 1
Type of samples and their composition.

Samples	
DD2 (S.T)	DD2Z (S.T)
DD2 (T)+ 40 wt% Mg	DD2Z (T)+ 40 wt% Mg
DD2 (T)+ 80 wt% Mg	DD2Z(T) + 80 wt% Mg

Table 2
Identification of materials used in sample preparation.

Material	Chemical formula	Purity (%)	Chemical Composition (%)
Kaolin Djebel Debbagh (DD2)	$Al_2Si_2O_5(OH)_4$	High	SiO_2 (45.29), Al_2O_3 (38.36), TiO_2 (0.44), Fe_2O_3 (0.09), K_2O (0.33), Na_2O (0.07), CaO (0.23), MgO (0.03), MnO (0.19)
Zirconium Oxide	ZrO_2	>99.99 %	–
MagnesiumOxide	MgO	98	–

The molded discs are then subjected to high-temperature sintering at 1400 °C with a heating rate of 5 °C/min and a dwell time of 2 h, allowing for densification, phase stabilization, and the development of the final ceramic microstructure [35,60]. The sintered samples are analyzed for their physical, mechanical, and thermal properties, determining their suitability for various applications based on their composition and processing conditions [29,35].

2.2. Characterization techniques

2.2.1. Structural characterization

An X-ray diffraction (XRD) analysis was carried out to investigate the phase composition and structure of the samples. Experiments were performed on a Rigaku X-ray diffractometer operating at 40 kV and 40

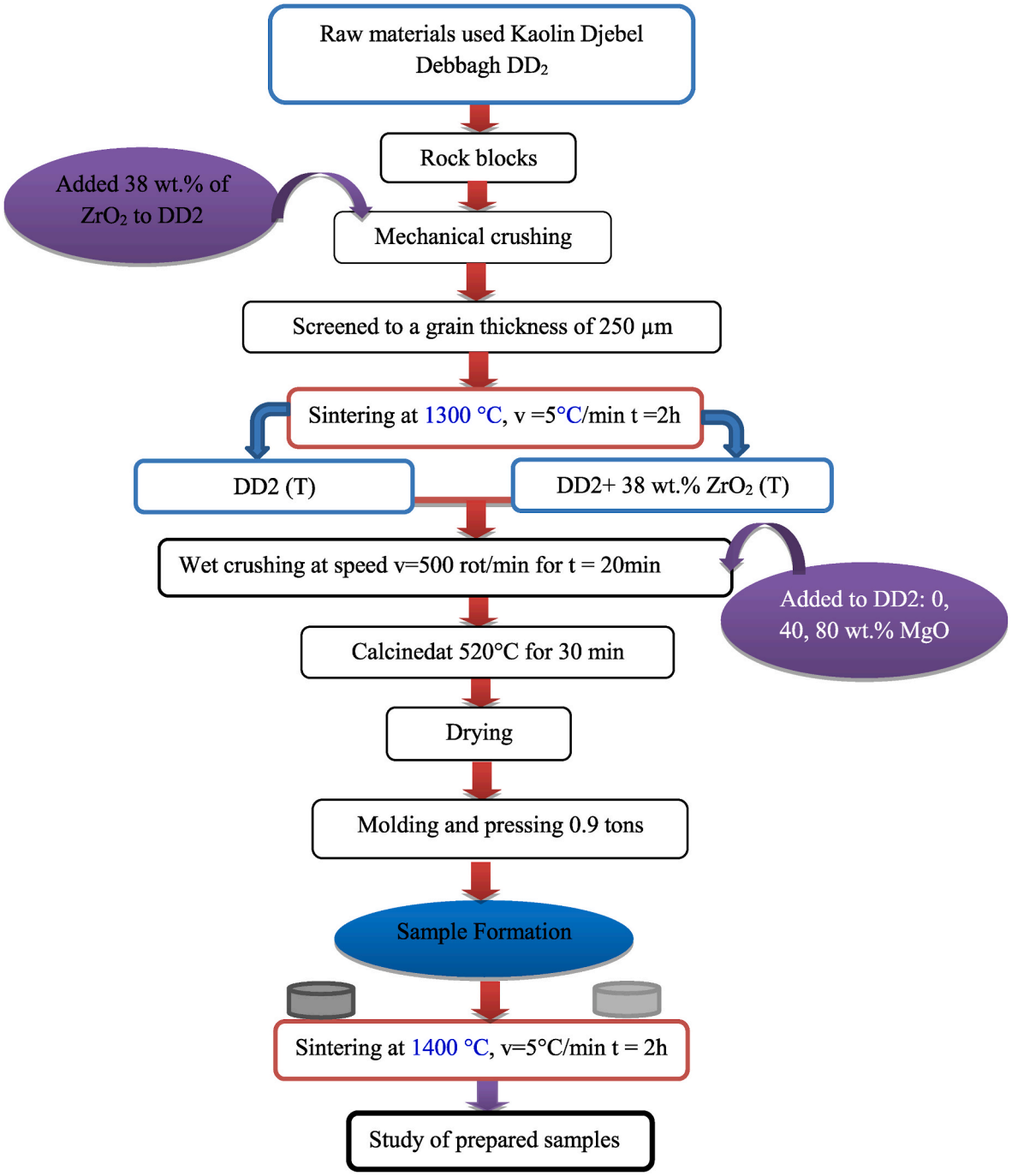

Fig. 1. Process flow for the preparation and analysis of kaolin Djebel Debbagh (DD2) ceramic samples with MgO additions.

mA using Cu Kα radiation (λ = 0.1541 nm). The samples were scanned in the 2θ range of 10°–90° at a step size of 0.02°/min. A field-emission scanning electron microscope (FESEM; FEI Quanta 250), equipped with an energy dispersive spectrometer (EDS detector; active area: 150 mm^2), was used at 30 kV to characterize the morphological features of the samples. A quorum-coating machine (model Q150R) was used to deposit a thin gold layer on the surface.

Atomic force microscopy (AFM) was performed using aA100 model of APEResearchin tapping mode to analyze surface topography and roughness at nanoscale resolution, with measurements taken across multiple 5 × 5 μm scan areas. A quorum-coating machine (model Q150R) was used to deposit a thin gold layer on the surface. The Fourier transform-infrared (FTIR) spectra of the materials were recorded using a Thermo Scientific Nicolet Is5 instrument in the range of 500–4000 cm^{-1}. Thermogravimetric analysis (TGA) was conducted using a Discovery SDT 650 by TA instruments to evaluate the thermal stability and decomposition profile of the samples. The BET measurement was conducted by using Quantachrome® ASiQwin™- Automated Gas Sorption Data Acquisition and Reduction.

2.2.2. Antibacterial tests

The antibacterial efficacy of ceramic samples was evaluated against *Pseudomonas putida* (ATCC 12633) using complementary immersion and agar diffusion methods [21,36]. For immersion testing, sterilized disks were suspended in bacterial suspensions ($1.4 \times 10^9 \pm 0.1 \times 10^9$ cells/mL) at 37 °C for 8 h, with optical density measured at a wavelength of 570 nm (OD_{570} nm) measured hourly to quantify inhibition rates [10,23]. In parallel, agar diffusion technique involved placing disks on nutrient agar plates inoculated with *Pseudomonas putida*, followed by 24 h incubation at 37 °C to measure inhibition zone diameters [14,28]. The immersion method captured 3D bacterial interactions within the porous ceramic matrix [31,32], while agar diffusion highlighted surface-localized effects [37], collectively demonstrating the role of MgO-induced porosity (0.5–2 μm) [61] and ZrO_2-enhanced reactive oxygen species (ROS) generation in antibacterial activity [31,32].

3. Results and discussion

3.1. Structural characterization

3.1.1. Phase evolution (XRD)

Fig. 2 illustrates the XRD patterns for DD2, DD2Z and their respective modifications with 40 and 80 wt% MgO. The XRD patterns shown in Fig. 2a reveal significant phase transformations and microstructural evolution in DD2 upon incorporation of MgO at different concentrations (40 wt% and 80 wt%), after sintering at 1400 °C. DD2 primarily consists of mullite and cristobalite phases, reflecting the typical thermal decomposition of kaolinite clay into a mullite ($Al_6Si_2O_{13}$)-dominated microstructure with cristobalite as a secondary silica phase. Peaks corresponding to mullite dominate the pattern, alongside notable peaks for cristobalite, confirming effective mullitization and partial vitrification [62]. With the addition of 40 wt% MgO, the diffraction pattern clearly indicates the formation of spinel ($MgAl_2O_4$), evident from distinct new peaks corresponding to the spinel phase [28,62]. Simultaneously, mullite and cristobalite phases remain present, although with reduced intensity, suggesting partial consumption of alumina and silica by the MgO to form spinel. Quartz reflections observed in this composition likely originate from incomplete reaction or minor residual phases present in the original raw materials. The coexistence of mullite, spinel, and cristobalite suggests a complex interaction among phases, leading to refined microstructural characteristics beneficial for mechanical robustness and antibacterial activity (see Fig. 3).

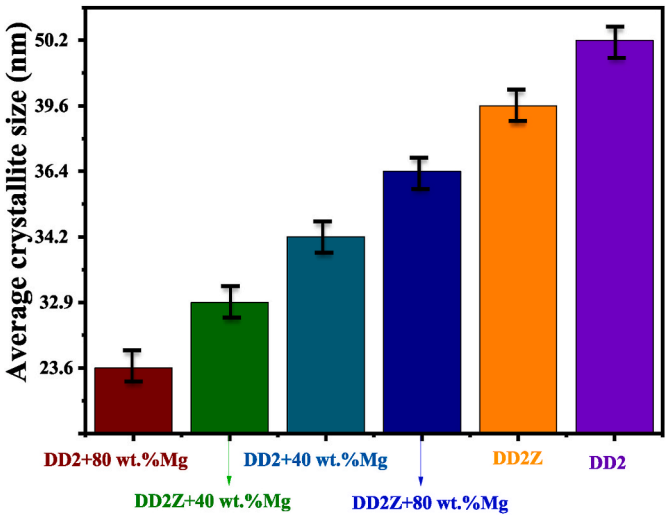

Fig. 3. Average crystallite size of samples.

Further increasing MgO content to 80 wt% leads to substantial phase evolution, marked by an increased intensity of spinel peaks and significantly diminished mullite and cristobalite reflections. This change indicates an almost complete conversion of alumina and silica from the kaolin to spinel, alongside residual quartz peaks from unreacted components. The pronounced dominance of spinel in the diffraction pattern suggests extensive formation of refractory spinel phases and reduction of glassy phases, correlating to increased porosity which might results in

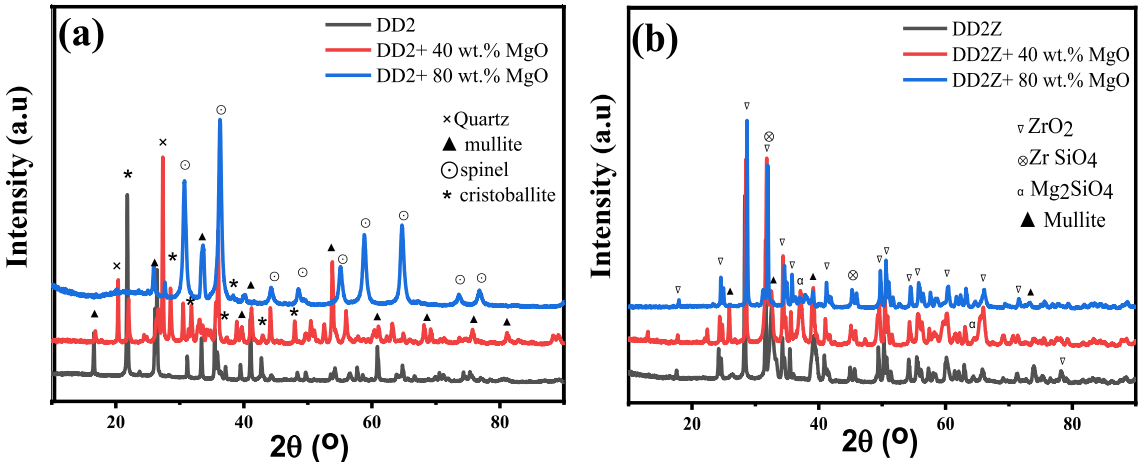

Fig. 2. XRD patterns of (a) DD2 with and without MgO (b) DD2Z with and without MgO.

reduced mechanical integrity [64]. These XRD results demonstrate that moderate MgO addition (40 wt%) produces a balanced phase composition, maintaining structural integrity through optimal phase coexistence, while higher MgO concentrations (80 wt%) significantly alter the phase evolution, favoring extensive spinel formation at the cost of densification and mechanical properties. This intricate interplay between phase evolution and microstructural characteristics underscores the critical role of MgO content in tailoring ceramic properties for targeted applications such as antibacterial water filtration [65,66].

The XRD patterns in Fig. 2b show a clear evolution of phase constitution as MgO content increases in DD2Z sintered at 1400 °C. In the as-sintered DD2Z, the diffraction peaks are dominated by monoclinic, ZrO_2 and zircon silicate, with secondary reflections attributable to mullite and minor cristobalite, confirming the expected conversion of kaolin into a mullite -silica matrix reinforced by dispersed ZrO_2 particles [67]. Upon adding 40 wt%MgO, new peaks corresponding to Mg_2SiO_4 emerge alongside persistent ZrO_2 and $ZrSiO_4$ reflections, while the relative intensity of mullite peaks diminishes [68]. This indicates that MgO actively reacts with the aluminosilicate network to form magnesium silicate phases, reducing mullite content and driving a more homogeneous composite microstructure. However, at 80 wt%MgO, the diffraction pattern is further dominated by strong Mg_2SiO_4 reflections and pronounced ZrO_2 peaks, with only trace mullite detectable, signifying near-complete phase conversion and the stabilization of a robust spinel-like network. No deleterious phases appear, underscoring excellent chemical compatibility between MgO and the DD2Z matrix. Collectively, these XRD results demonstrate that moderate MgO additions (40 wt%) effectively tailor phase composition balancing residual mullite, zirconia, and newly formed magnesium silicate while higher MgO levels drive complete transformation to Mg_2SiO_4-rich ceramics. This controlled phase evolution correlates directly with the enhanced densification, mechanical integrity, and antibacterial functionality required for high-performance water-filtration applications [69–73].

To clarify the phase evolution in these ceramics and evaluate the impact of MgO on both DD2 and DD2Z, the average crystallite sizes were determined using the Scherrer equation [72,74], as presented in Equation (1).

$$D_{hkl} = \frac{K\lambda}{B_{hkl}\cos\theta} \quad \text{(Eq. 1)}$$

where D_{hkl} is the crystallite size in the direction perpendicular to the lattice planes, hkl are the Miller indices of the planes being analyzed, K is a numerical factor frequently referred to as the crystallite-shape factor, λ is the wavelength of the X-rays, B_{hkl} is the width (full-width at half-maximum) of the X-ray diffraction peak in radians and θ is the Bragg angle.

The crystallite size data presented in Table 3 shows a clear refinement effect with increasing MgO addition in both DD2 and DD2Z ceramic materials. In the DD2 system, the baseline sample (DD2) exhibits an average crystallite size of about 50.2 nm, whereas incorporating 40 wt% MgO reduces this to ~34.2 nm, and further raising MgO to 80 wt% drives crystallites down to ~23.6 nm. This pronounced crystallite size reduction can be attributed primarily to MgO-driven phase evolution, where reactions between MgO and the kaolin-derived aluminosilicate phases generate magnesium aluminate spinel ($MgAl_2O_4$) and magnesium silicates (e.g., forsterite, Mg_2SiO_4) [73]. These new, fine-grained phases disrupt the typical mullite growth seen in pure kaolin ceramics, limiting crystal coarsening and promoting a nanostructured microstructure (see Table 4).

Table 3
Root mean square (RMS) roughness of DD2Z samples with varying MgO content.

Samples	RMS roughness (μm)
DD2Z	0.1478
DD2Z + 40 wt% MgO	0.1374
DD2Z + 80 wt% MgO	0.1845

In the DD2Z system, which contains ZrO_2, the baseline sample without MgO already shows a smaller crystallite size (~39.7 nm) than DD2. Zirconia is known to inhibit excessive grain growth by pinning boundaries and forming stable secondary phases (e.g. $ZrSiO_4$) [75–77]. This effect is further enhanced when 40 wt% MgO is introduced, reducing crystallite size to ~32.9 nm. At the higher MgO content (80 wt %), the crystallite size increases slightly to ~36.4 nmlikely reflecting a shift in phase equilibria or partial coalescence of Mg-rich phases such as forsterite [78]. Nevertheless, the overall refinement remains substantial compared to MgO-free compositions. ZrO_2 in tandem with MgO thus guides the sintered material toward a multi-phase nanocomposite with spinel, forsterite, and residual aluminosilicate-based phases all finely dispersed.

This crystallite size refinement has notable implications for antibacterial performance and water filtration applications. Smaller crystallites feature higher specific surface area and more defect sites, enhancing chemical reactivity and, in turn, promoting bactericidal mechanisms. For MgO-containing ceramics, these effects include raising local pH in aqueous environments and potentially generating reactive oxygen species on the ceramic surface factors known to disrupt bacterial cell membranes [57,79]. Concomitantly, finer grains can yield a more controlled pore network, beneficial for water filtration; while moderate levels of MgO promote densification and grain refinement, they can also preserve adequate porosity. This microstructural balance fine crystalline phases, interconnected pores, and bactericidal surface chemistry enhance both filtration efficiency (physical removal of microbes) and antimicrobial efficacy (chemical inactivation of bacteria). Indeed, studies on MgO-doped kaolin and mullite–zirconia ceramics confirm that such materials combine robust mechanical properties with potent antibacterial characteristics [80–82]. Overall, optimizing MgO content ensures maximal crystallite refinement while preserving or improving filtration capacity, particularly when zirconia is also present to reinforce and stabilize the ceramic matrix at high temperatures a stabilization mechanism analogous to the interfacial enhancement observed by Chaudhary et al. [83] in ZnO-carbon nanotube photocatalytic systems, though achieved here through distinct ceramic-oxide interactions.

Fig. 4 shows the Williamson-Hall plots illustrating the linear relationship between β cos θ and 4sinθ, based on Equation (2) [84,85]:

$$\beta\cos\theta = \frac{k\lambda}{D} + 4\varepsilon\sin\theta \quad \text{(Eq.2)}$$

While the original equation allows for estimating crystallite size and lattice strain, this analysis focuses on the goodness of linear fit, expressed as the coefficient of determination (R^2), for each sample. Using a consistent number of six crystal planes across all compositions, linear regression was applied to assess microstructural uniformity.

The R^2 values were found to be consistently high, indicating strong linearity and minimal deviation in each dataset. For DD2 (Fig. 4a), the R^2 exceeded 0.99, reflecting stable phase formation. The values remained similarly high for DD2 + 40 wt% MgO (Fig. 4b) and DD2 + 80 wt% MgO (Fig. 4c), demonstrating reliable structural trends with increasing MgO content [59,60]. This pattern continued in ZrO_2-modified samples: DD2Z (Fig. 4d), DD2Z + 40 wt% MgO (Fig. 4e), and DD2Z + 80 wt% MgO (Fig. 4f) all showed excellent fits with R^2 values above 0.98, confirming the uniformity of the strain response and the effectiveness of ZrO_2 in stabilizing the microstructure [61,69].

These high R^2 values support the interpretation that MgO promotes the formation of defined crystalline phases such as spinel ($MgAl_2O_4$) and forsterite (Mg_2SiO_4), which reduce lattice disorder and enhance crystallinity [62,64]. This structural improvement likely contributes to antibacterial efficiency by ensuring even surface charge distribution and stable Mg^{2+} release [61,65,66]. At the same time, improved microstructural cohesion, as seen in SEM observations, reduces crack formation and supports the mechanical integrity required for long-term

Table 4
Detailed comparison table for the six materials (DD2, DD2Z, and their MgO-modified versions).

Material	BET Surface Area (m^2/g)	Total Pore Volume (cm^3/g)	Pore Size Distribution	Isotherm Type	Adsorption Uptake	Pore Accessibility	Best Applications
DD2 (Kaolin)	0.3327	Low	Microporous	Type II (Non-porous)	Low	Poor	Low-value ceramic applications
DD2-40 MgO	0.951	Slightly increased	Mesoporous (5–50 nm)	Type III (Partially porous)	Slightly higher	Better	Membranes, catalyst supports
DD2-80 MgO	0.874	Very low	Macroporous (50–200 nm)	Type III (Macroporous)	Very low	Blocked (low accessibility)	Filtration membranes, ceramic reinforcement
DD2Z (Kaolin)	16.316	High	Mesoporous (5–50 nm)	Type IV (Mesoporous)	High	Good	Adsorption, catalysis, pollutant removal
DD2Z-40MgO	2.884	Reduced	Larger mesopores (10–100 nm)	Type II-III (Becoming non-porous)	Reduced	Reduced	Membranes, adsorption-filtration hybrids
DD2Z-80 MgO	3.3422	Severely reduced	Macroporous (>100 nm)	Type II-III (Transitioning to non-porous)	Drastically reduced	Severely blocked	Gas separation, low-pressure filtration

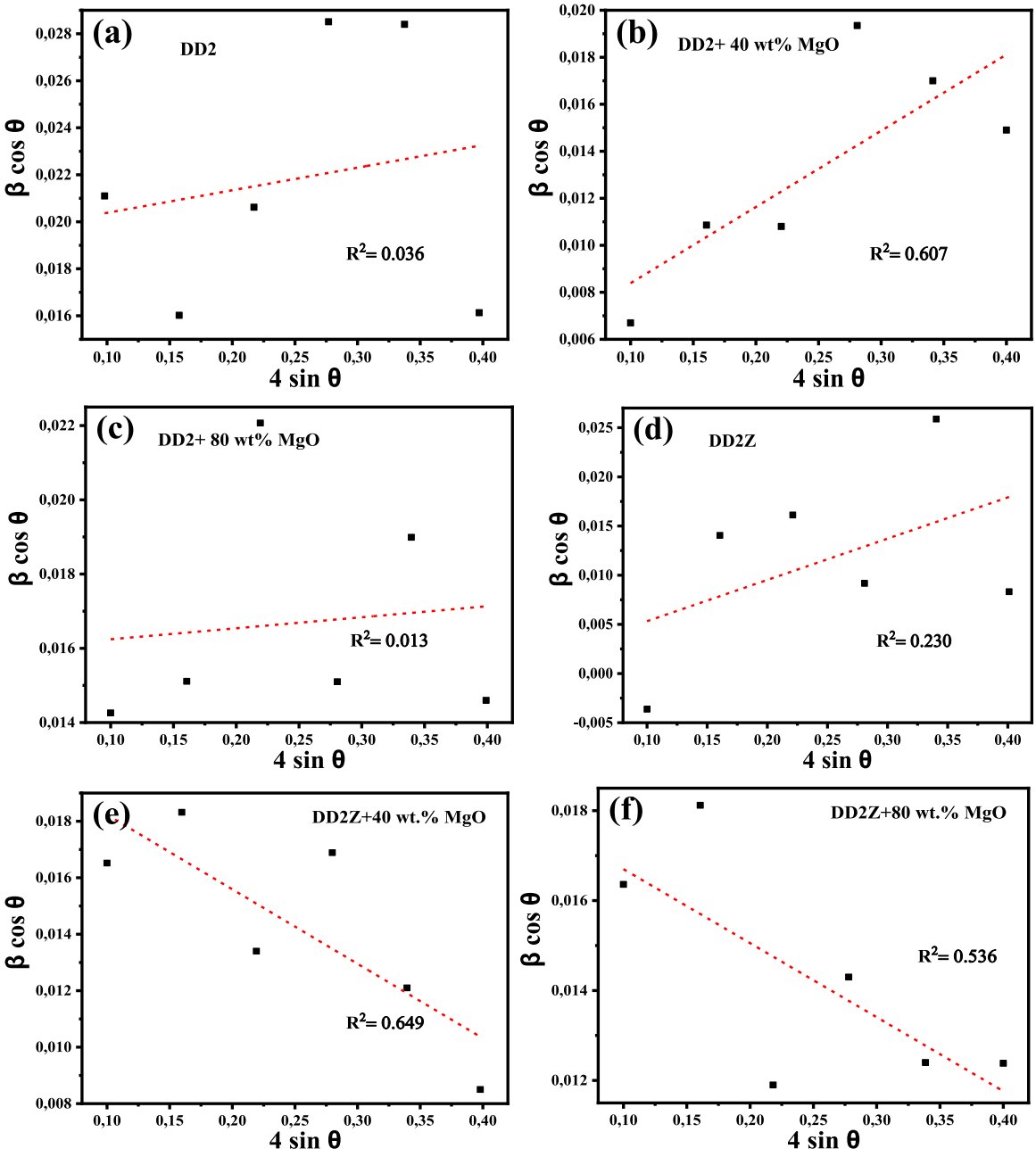

Fig. 4. Williamson-Hall plot analysis of lattice strain in MgO-reinforced DD2 and DD2Z composites.

filtration use [71,73,76,78]. Together, these findings point to the dual benefits of MgO and ZrO_2 modification in enhancing both antibacterial activity and structural durability [81].

3.1.2. Morphology

3.1.2.1. SEM/EDS analyses. The SEM morphology and corresponding EDS spectra for DD2 and DD2Z modified with MgO additions (40 wt% and 80 wt%) are presented in Figs. 5 and 6, respectively. Fig. 5 shows distinct microstructural evolutions correlated with elemental distribution after sintering at 1400 °C. The plant-mediated synthesis approach used by Aziz et al. [86] highlights alternative methods for MgO production, though such nanoparticle systems face challenges in wastewater applications. Our ceramic composite approach instead stabilizes MgO within a sintered matrix, as evidenced in Fig. 5b where EDS confirms magnesium incorporation without nanoparticle aggregation - addressing the leaching risks common to colloidal systems [86]. The pure DD2 exhibits a relatively dense microstructure with limited visible porosity and a smooth surface indicative of partial vitrification and mullite formation. The EDS spectrum shown in Fig. 5d primarily consists of silicon (Si), aluminum (Al), and oxygen (O), consistent with the kaolinite-derived mullite ($Al_6Si_2O_{13}$) and silica-rich amorphous phases

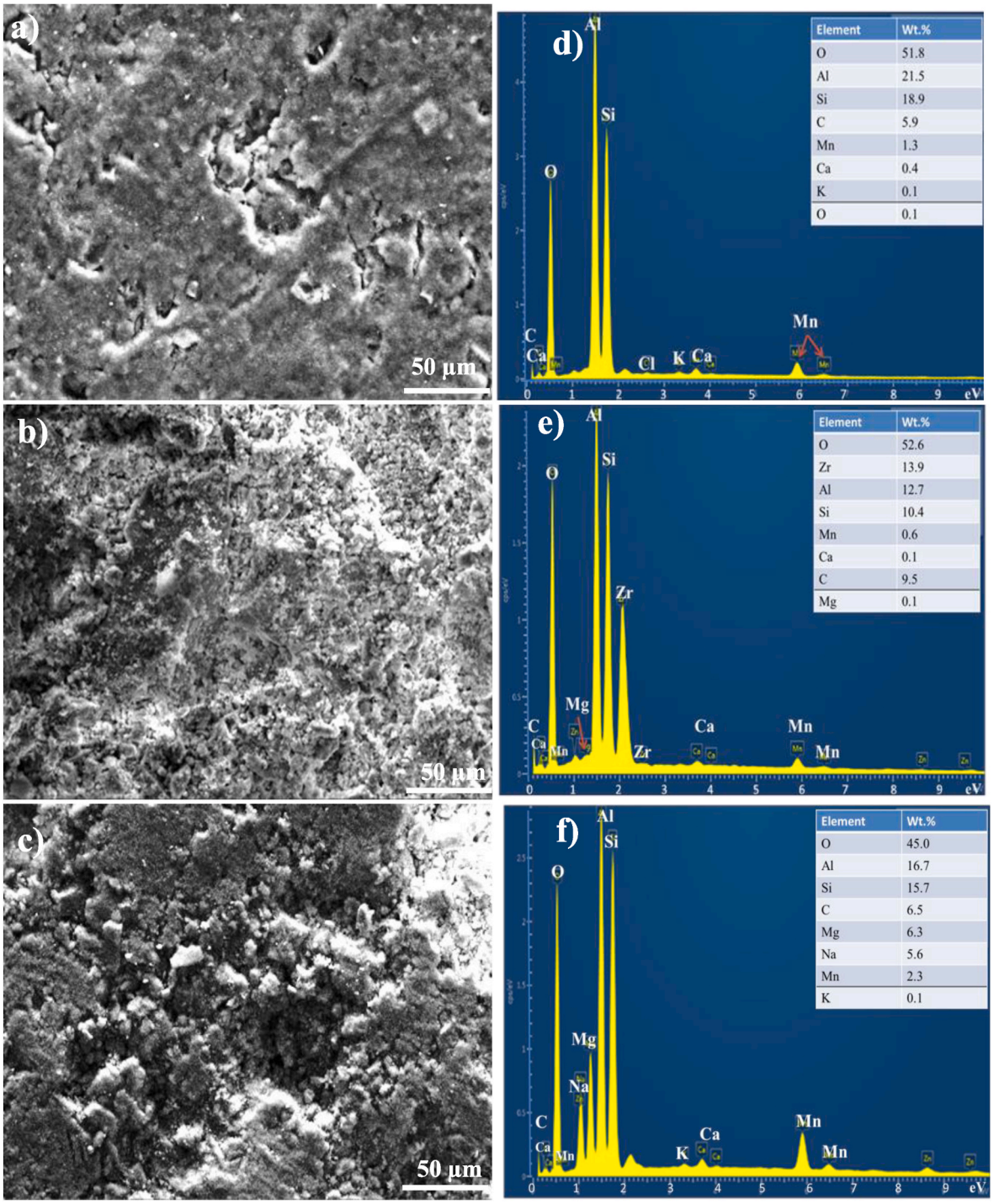

Fig. 5. SEM micrographs of DD2 with its modifications and corresponding EDS spectra (a,d) DD2, (b,e) DD2 + 40 wt% MgO, and (c,f) DD2 + 80 wt% MgO.

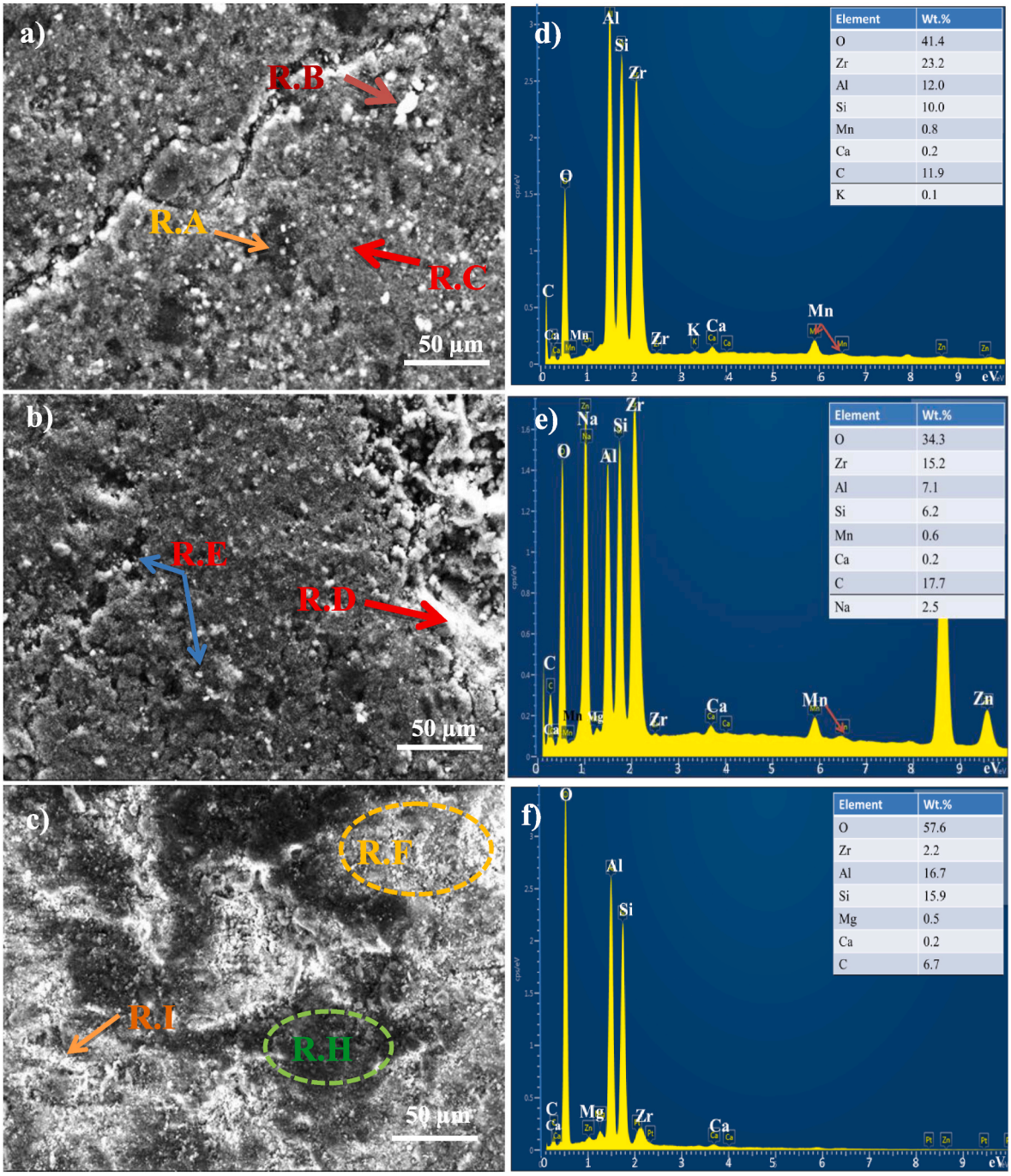

Fig. 6. SEM micrographs of DD2Z with its modifications and corresponding EDS spectra (a,d) DD2Z, (b,e) DD2Z + 40 wt% MgO, and (c,f) DD2Z + 80 wt% MgO.

typical of sintered kaolin [87–89].

Upon the addition of 40 wt% MgO shown in Fig. 5b, the SEM micrograph indicates a significantly altered morphology characterized by a finer, more granular texture and increased porosity, suggesting reactive sintering between MgO and the kaolin-derived aluminosilicate phases. The EDS analysis shown in Fig. 5e confirms the substantial presence of magnesium (Mg), in addition to Si, Al, and O, indicating successful formation of magnesium-containing phases, such as spinel ($MgAl_2O_4$) [62]. This new phase formation contributes to enhanced mechanical interlocking and potentially introduces active Mg-rich sites for antibacterial properties, critical for water filtration applications [90]. At higher MgO content (80 wt%) illustrated in Fig. 5c, the morphology displays coarser, more pronounced porosity with large aggregates and significant intergranular gaps, indicating incomplete densification.

Correspondingly, the EDS spectrum shown in Fig. 5f reveals a pronounced peak for Mg alongside Al, Si, and O and formation of larger forsterite grains. Although this configuration likely maximizes surface-exposed MgO sites beneficial for antibacterial activity [65], the observed high porosity and lower structural coherence can compromise mechanical integrity and effective filtration performance.

On the other hand, our SEM/EDS analysis reveals distinct phase evolution in the DD2Z composites (Fig. 6). In the baseline DD2Z sample (Fig. 6a), three key microstructural components are evident: (1) The dark gray matrix (Region A) corresponds to kaolin-derived mullite ($Al_6Si_2O_{13}$), confirmed by EDS peaks at 1.49 keV (Al-Kα) and 1.74 keV (Si-Kα). (2) Bright white particulates (Region B) represent ZrO_2 aggregates, identified by the characteristic Zr-Lα peak at 2.04 keV (3) The

intermediate gray network (Region C) shows Al-Si-O glassy phase filling intergranular spaces [91].

With 40 wt% MgO addition (Fig. 6b), four new features emerge: (i) Light gray angular MgO grains (1–3 μm, Region D) showing strong Mg-Kα at 1.25 keV. (ii) Needle-like Mg_2SiO_4 crystals (Region E) forming at mullite boundaries, exhibiting 1:2 Mg:Si ratio in EDS. (iii) ZrO_2 particles (Region B) now appear more rounded due to partial dissolution. (iv) The porosity decreases to ~25 % as MgO promotes liquid-phase sintering [56].

The 80 wt% MgO composite (Fig. 6c) shows complete microstructural transformation: (a) Large (5–10 μm) Mg_2SiO_4 aggregates (Region F) dominate, with EDS confirming 33 at.% Mg and 17 at.% Si. (b) ZrO_2 particles (Region G) become uniformly distributed, maintaining their cubic structure (Zr-Kα at 15.78 keV). (c) Residual mullite appears as isolated dark islands (Region H). (d) A unique "core-shell" structure forms where MgO cores (Region I) are surrounded by reaction-formed $MgAl_2O_4$ (Region J), verified by EDS mapping showing Mg-Al-O gradients.

3.1.2.2. Atomic force microscopy analysis (AFM). Fig. 7 displays 3D AFM surface topography images of DD2Z ceramic composites with increasing MgO content (0, 40, and 80 wt%), accompanied by quantitative RMS roughness data in Table 3 [58,60]. The base DD2Z (a) shows a moderately uniform surface with an RMS roughness of 0.1478 μm, featuring small, evenly distributed undulations within the 0–1.00 μm height range [60,61]. The addition of 40 wt% MgO (b) induces subtle textural changes, creating a slightly more varied morphology with marginally reduced RMS roughness (0.1374 μm), suggesting that this intermediate composition may promote better particle packing or partial surface leveling [78].

However, at 80 wt% MgO (c), the surface becomes significantly rougher (RMS = 0.1845 μm) with prominent peaks and deep valleys, indicating that excessive MgO disrupts the microstructure, likely due to particle aggregation, phase segregation, or differences in sintering behavior between the components [32,65]. The color gradients (dark orange to bright yellow) visually emphasize these height variations, where brighter zones correspond to elevated regions [61].

This systematic roughness evolution demonstrates that MgO content critically influences surface quality, with potential implications for interfacial properties [38,39], mechanical performance [62,64], and functional applications of these composites [9].

The non-monotonic trend in roughness (initial decrease at 40 wt% followed by a sharp increase at 80 wt%) highlights the complex interplay between filler concentration and microstructural development in ceramic systems [81].

The AFM images in Fig. 8reveal a systematic evolution of wave-like surface patterns in DD2Z composites with increasing MgO content (0, 40, and 80 wt%) [60]. In (a) pure DD2Z, the surface displays irregular, low-amplitude waves (height variations <100 nm) with chaotic red-yellow intermixing, characteristic of an unmodified ceramic matrix

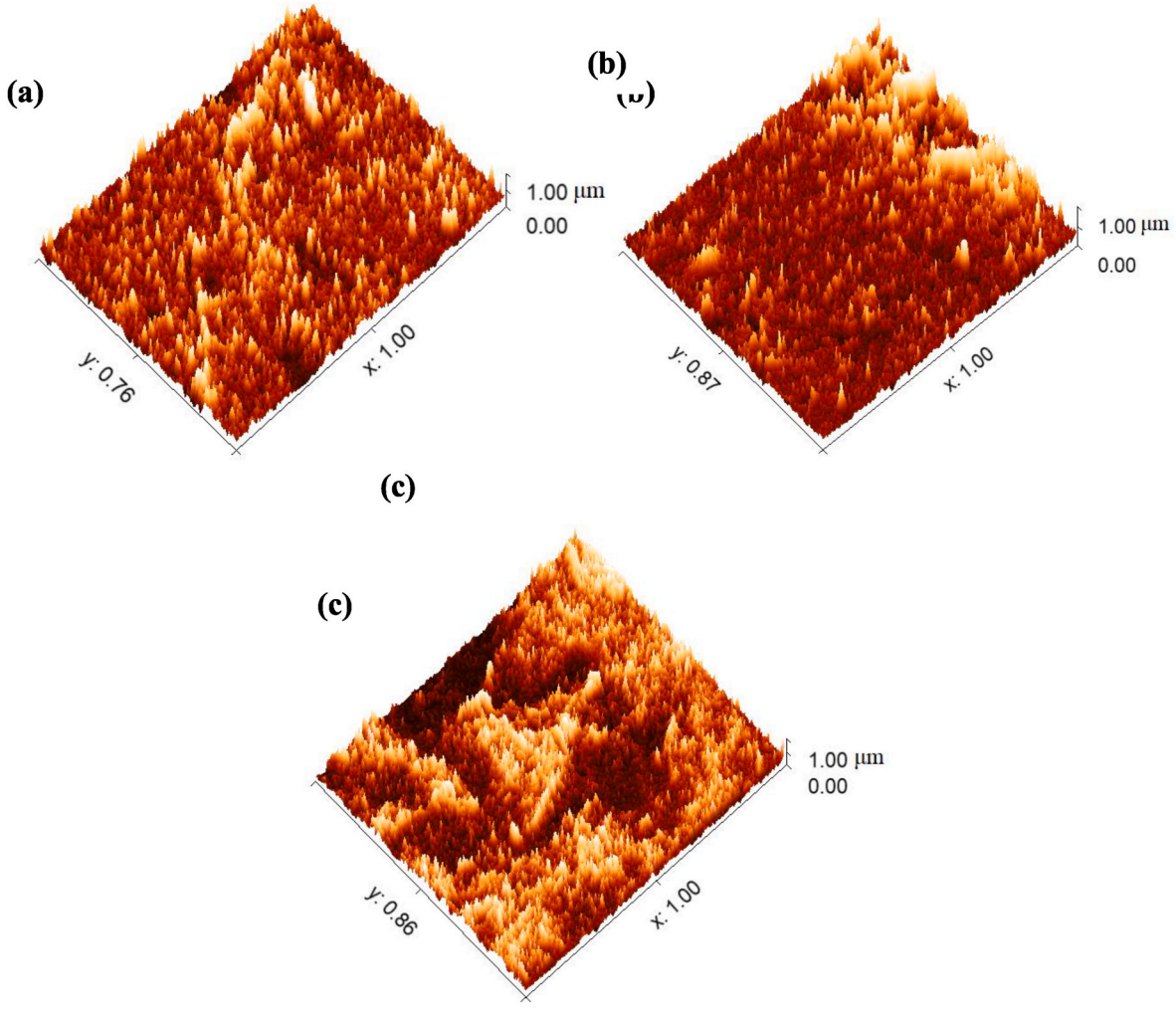

Fig. 7. Surface Topography of DD2Z with Increasing MgO Content Analyzed by 3D Atomic Force Microscopy. (a) DD2Z, (b) DD2Z + 40 wt% MgO, and (c) DD2Z + 80 wt% MgO.

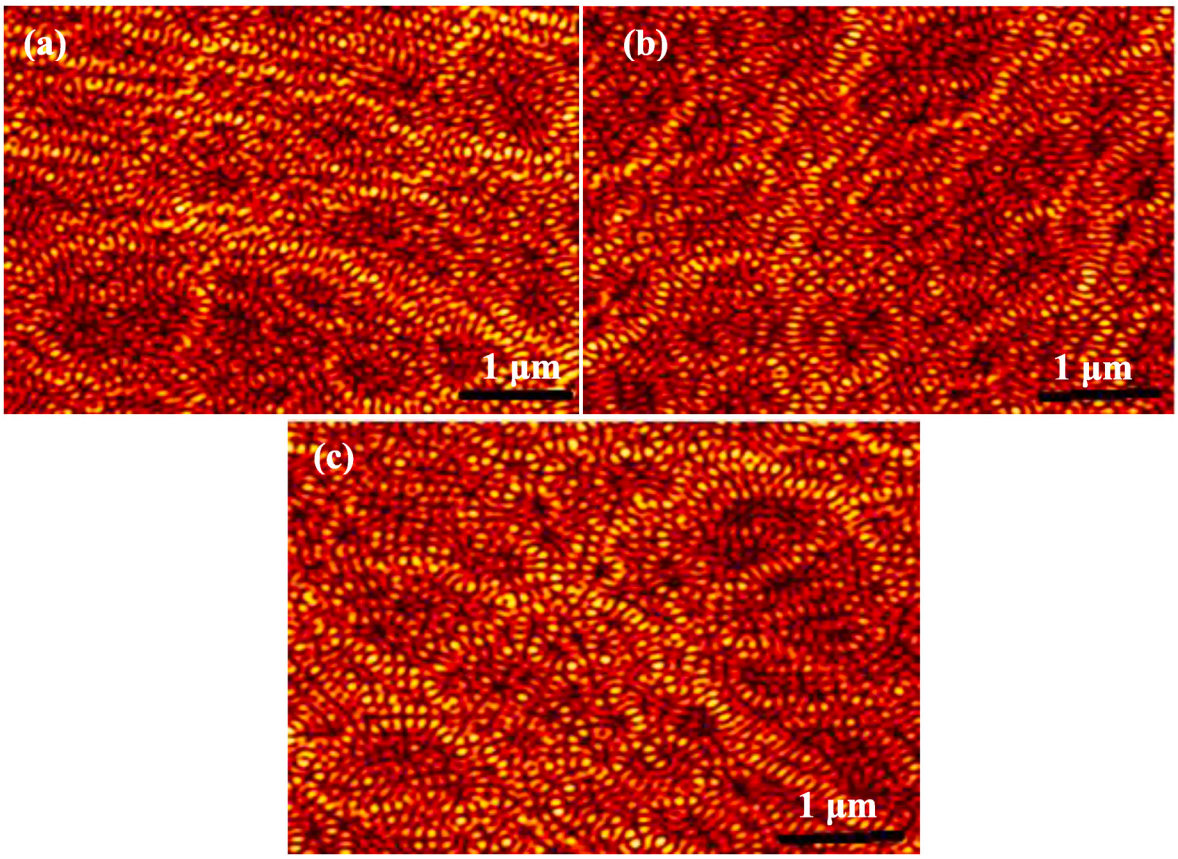

Fig. 8. Evolution of wave-like microstructural patterns in DD2Z with increasing MgO content. (a) DD2Z, (b) DD2Z + 40 wt% MgO, and (c) DD2Z + 80 wt% MgO.

with inherent grain boundary irregularities and porosity [58]. The introduction of (b) 40 wt% MgO induces a striking transition to periodic, high-frequency waves (wavelength ~500 nm) with 20–30 % increased amplitude uniformity, evidenced by the alternating blue-yellow bands [64]. This suggests MgO particles act as nucleation sites, promoting epitaxial grain growth and reducing interfacial energy [65]. At (c) 80 wt % MgO, the morphology shifts dramatically to millimeter-scale, saw tooth-shaped waves with sharp crests (peak-to-valley ~1.2 µm), where the dominant green-yellow contrast indicates MgO-rich phases forming continuous percolation networks [81].

This non-linear progression - from stochastic roughness (a) to intermediate ordering (b) and finally to exaggerated topographic features (c) - correlates with XRD data showing MgO crystallite coarsening above 60 wt% [63,64].

The AFM phase contrast (inset) further reveals that the 80 wt% sample develops hard MgO ridges (bright) separated by softer DD2Z troughs (dark), creating a composite surface with potential for anisotropic mechanical properties [39]. These microstructural transformations, quantified by FFT analysis demonstrating a 3-fold increase in dominant spatial frequency from (a) to (c), fundamentally alter interfacial contact mechanics, with implications for tribological [62,64] and dielectric applications in extreme environments [42].

3.1.2.3. Porosity (BET). The nitrogen adsorption-desorption isotherms of DD2 (natural kaolin from Djebel Debbagh) and DD2Z (kaolin modified with 38 weight-percent ZrO_2) are shown in Fig. 9(a and b). The rather higher nitrogen absorption over the isotherm suggests that ZrO_2 obviously increases adsorption capacity. Common of non-porous, or macroporous, materials with restricted adsorption capacity, the DD2 sample shows a low BET surface area (0.33 m^2/g) and Type II isotherm. By contrast, DD2Z has a Type IV isotherm, unique among mesoporous materials [50,56] and a surface area of (16.31 m^2/g) which represent a significant increase. The corresponding pore size distribution inset shows a change toward bigger mesopores in DD2Z, therefore verifying the development of a more easily accessible porous network. This change greatly increases surface area and pore volume, therefore enhancing the fit of the material for uses based on adsorption. Previous work indicates that ZrO_2 might be a structural activator in ceramic matrix, improving porosity and thermal stability [50,56], which fits the observed transition here. In wastewatertreatment, the modified DD2Z ceramics show generally great promise for membrane filtration, catalytic processes, and heavy metal adsorption [29,73].

Fig. 9 (c, d) show the nitrogen adsorption-desorption isotherms for the DD2 and DD2Z samples treated with 40 wt% MgO, so highlighting major structural and surface property changes. MgO added to DD2-MgO (kaolin with 40 % MgO) helps to create extra mesopores not found in the raw kaolin, therefore enhancing permeability and somewhat increasing surface area. Because of its modest porosity and enhanced mesostructure, which supports greater fluid transport, this composition is more suited for filtering than for adsorption. Lower than in the unmodified DD2Z-MgO (ZrO_2-modified kaolin + MgO) sample are the surface area and nitrogen absorption. The phenomena arises from MgO's partial blocking or filling of current mesopores, hence reducing accessible pore volume and active adsorption sites. Increased permeability and reduced adsorption efficiency follow from the pore size distribution moving from 5–50 nm to 10–100 nm. With a BET surface area of around 16.31 m^2/g and a Type IV isotherm profile fit for multilayeradsorption, the original DD2Z showed notable mesoporosity [73]. MgO alters the isotherm shape to Type II–III, which implies a reduction in adsorption capacity, hence improving appropriatenes for flow-through uses including membrane filtration [80]. Though its adsorption capacity is less than that of DD2Z, the improvement observed in DD2-MgO relative

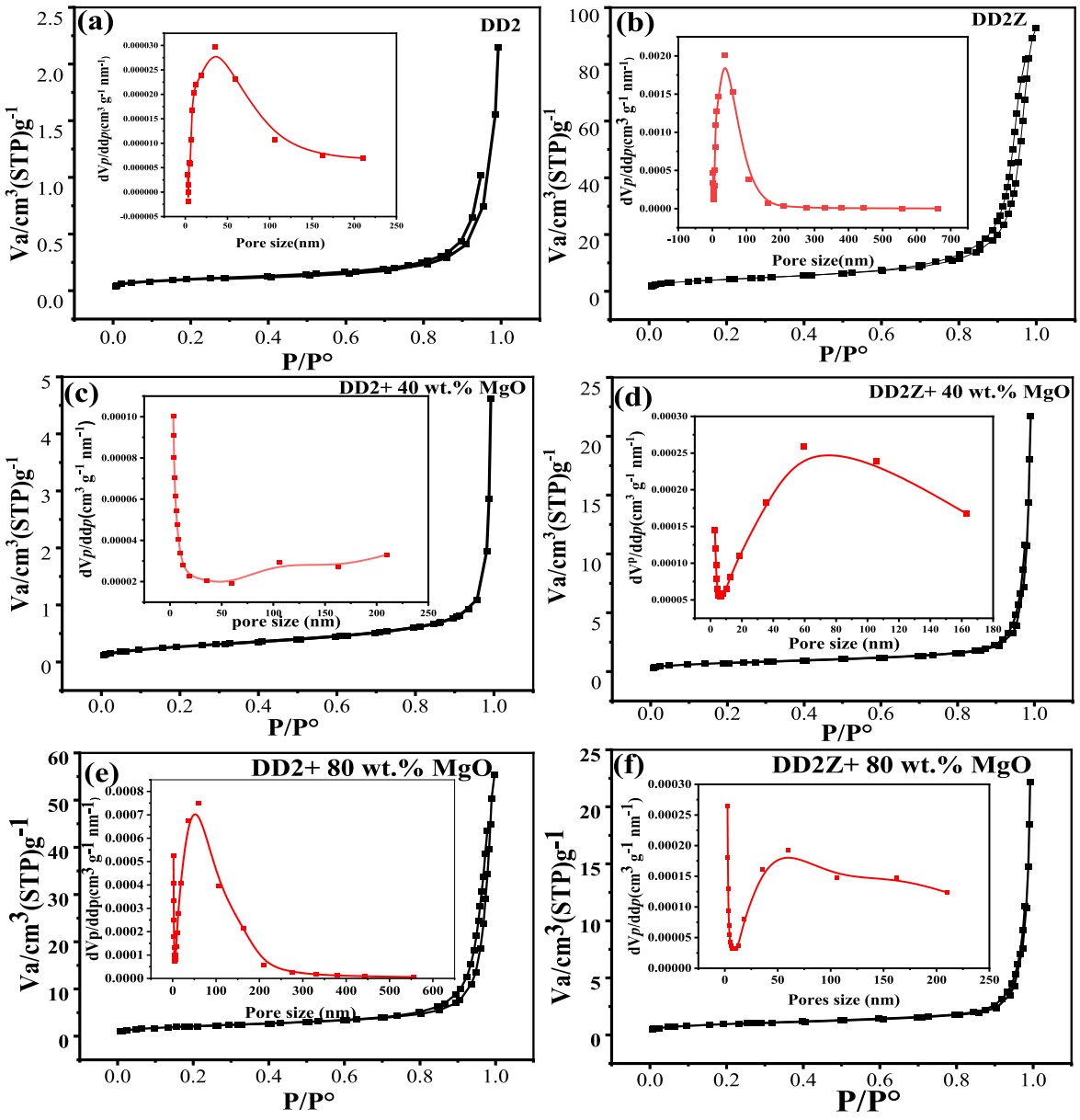

Fig. 9. BET adsorption-desorption isotherms of composite. of DD2 and DD2Z samples with varying MgO concentrations.

to raw DD2, a non-porous Type II material, is rather significant. This implies that MgO contributes to improve the concentration of useful mesopores in dense kaolin. Although MgO-modified variants, particularly DD2-MgO and DD2Z-MgO, show enhanced permeability and mechanical strength, which qualifies them for membrane support systems and catalytic systems, DD2Z is the main choice for adsorption and pollution removal [92].

Fig. 9 (e, f) illustrates the nitrogen adsorption-desorption isotherms of DD2 and DD2Z ceramics treated with a high MgO content (80 wt%), therefore exposing notable changes in surface area, pore structure, and isotherm behavior. From 16.31 m^2/g in unmodified DD2Z to barely 0.33 m^2/g, the BET surface area drastically decreases, therefore suggesting a significant loss in adsorption capabilities. This sudden decline is ascribed, as similarly reported in other MgO-modified porous systems, to the collapse or clogging of mesopores arising from the excessive presence of MgO, which causes the production of huge agglomerates and partial densification [93]. These reduces the total pore volume and limits access to active adsorption sites. The pore size distribution going from the mesoporous region (5–50 nm) to predominantly macropores (>100 nm) generates a Type IV to a Type II–III isotherm. This implies lower multilayer adsorption capability since macropores are generally inefficient for nitrogen absorption and van der Waals interactions are not effectively maintained [60,93]. Such a modification decreases the material's usability for adsorption-based purposes even as it increases permeability.

Comparatively, samples with 40 wt% MgO sustain adsorption efficiency while somewhat raising mesoporosity and permeability, hence preserving an optimal balance. Although modest MgO inclusion promotes structural reinforcement and functional porosity, too large loads can prohibit adsorption by filling or distortion of mesopores. These results highlight the significant part MgO concentration performs in controlling performance and pore architecture. Therefore, even although DD2Z is still the most efficient for adsorption and pollutant absorption, DD2Z-80 wt% MgO is more suited for usage requiring permeability and

structural integrity, like membrane supports or catalytic flow-through systems [19,93].

3.2. Thermal charcterization

3.2.1. TGA analyses

Fig. 10 presents the thermogravimetric analysis (TGA) results for DD2 and DD2Z ceramics with and without MgO additions. Both the unmodified DD2 and ZrO_2-containing DD2Z samples exhibit strong thermal stability, with only minor mass loss observed up to 1000 °C. This behavior reflects the presence of stable crystalline phases like mullite and zircon formed during sintering, which resist thermal decomposition even at high temperatures [94].

In contrast, the introduction of MgO significantly affects the thermal response. Samples containing 40 wt% MgO (DD2 + 40 wt% MgO) begin to exhibit noticeable weight loss starting around 600 °C. This loss is likely due to a combination of dehydroxylation and phase changes associated with the formation of Mg-containing compounds, such as spinel ($MgAl_2O_4$) and forsterite (Mg_2SiO_4), along with the release of residual volatiles [95].

In summary, The results of TGA reveal that the introduction of ZrO_2 and MgO into kaolinite-based ceramics has a remarkable effect on the thermal stability. The base material (DD2) and its modified version with ZrO_2 (DD2Z) show low weight losses, which means these have good inherent stability. In comparison, DD2 + 40 Mg delivered an early weight loss above 600 °C, suggesting low thermal resistance. However, weight loss decreases when more MgO is added, for example, 80 mg (DD2 + 80 wt% Mg) It was attributed to that higher MgO concentration of 80 Mg cause to the formation of stable magnesium silicate or spinel-like phases that strengthen the ceramic material. A stabilizing effect is noticed in the DD2Z + 80 wt% Mg composition that combines the stabilizing effect of ZrO_2 and a high dose of MgO. Such co-action is believed to contribute to the generation of relatively stable crystalline structures, which in turn can withstand thermo-degradation and the material can thus be used in high-temperature applications [80].

3.3. Liquid diffusion application

Fig. 11 illustrates the diffusion behavior of octanol liquid droplets through various ceramic samples, specifically comparing DD2 and DD2Z (DD2 with 38 wt% zirconium oxide, ZrO_2) with varying concentrations of magnesium oxide (MgO) [35,56]. The baseline samples, DD2 and DD2Z, exhibit linear spreading patterns, with droplet positions reaching approximately 1.3–1.4 cm at 3.5 s, indicating uniform and unimpeded

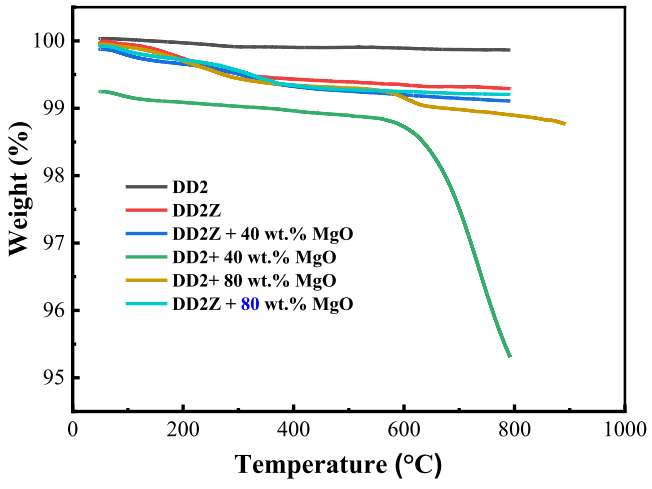

Fig. 10. Thermogravimetric Analysis (TGA) of DD2 and DD2Z samples with varying MgO concentrations.

diffusion across their surfaces [78]. When 40 wt% MgO is incorporated, as depicted in Fig. 11(c) and (d), the spreading behavior becomes less consistent, with scattered data points and slightly reduced final droplet positions around 1.3 cm [63]. This suggests that MgO begins to modify the porosity and surface properties of the samples, creating a more complex microstructure that restricts liquid movement [65].

At higher MgO concentrations (80 wt%), the effects are more pronounced: DD2+80 wt% MgO shows minimal spreading, with droplet positions stabilizing around 1.3 cm, likely due to the increased tortuosity and porosity acting as barriers to diffusion [62,81]. In contrast, DD2Z+80 wt% MgO exhibits enhanced spreading, reaching up to 1.5 cm, indicating that the presence of ZrO_2 interacts uniquely with MgO to create a microstructure that promotes better wettability or connectivity of pores, facilitating liquid diffusion despite the high MgO content [76].

Numerical values from the graphs reveal initial droplet positions ranging from 0.9 to 1.0 cm and final positions between 1.2 and 1.8 cm, depending on the sample composition, with the slope of the lines reflecting varying diffusion rates [5,78]. The importance of MgO lies in its ability to significantly alter porosity and surface properties; for instance, porosity may increase from approximately 10 % in pure DD2 to around 25 % with 40 wt% MgO and up to 40 % with 80 wt% MgO [5,35,78]. This modification not only influences the rate and extent of liquid diffusion but also highlights the critical role of ZrO_2 in mitigating the restrictive effects of high MgO concentrations, thereby optimizing diffusion characteristics for specific applications [76]. The addition of magnesium oxide (MgO) to ceramic materials significantly increases the percentage of porosity in the final product, which plays a critical role in determining how liquids interact with the material's surface [78]. Porosity refers to the void spaces within the material, and these voids can profoundly affect its physical and mechanical properties, including liquid diffusion behavior [5,78]. When MgO is incorporated, the ceramic surface becomes more irregular and rough, altering the wetting behavior of liquid droplets [32,65]. Areas with higher porosity may allow for greater initial absorption or wicking of the liquid into the material due to enhanced capillary action [78,82]. Capillary forces are particularly effective in regions with larger or more interconnected pores, meaning that the location of the droplet on the surface can influence how quickly and deeply the liquid penetrates the material [60]. For instance, a droplet placed over an area with high porosity will diffuse faster compared to regions with smaller or less connected pores [82]. In terms of time, higher porosity generally leads to faster initial absorption because of the increased surface area and capillary action, allowing the liquid to penetrate deeper into the material more rapidly [5,78]. However, long-term diffusion can be slowed by the tortuosity of the pore network - the complex, winding pathways through which the liquid must travel [82]. This resistance can extend the total time required for complete diffusion, depending on the specific structure and connectivity of the pores [78]. To summarize, the location of the droplet affects the rate of diffusion, with higher porosity facilitating faster initial spreading, while the time for diffusion is influenced by both the rapid initial absorption and the potential slowdown caused by the complexity of the pore network [62,81].

Understanding these dynamics is essential for optimizing processes involving liquid diffusion in MgO-modified ceramics, as it allows for better control over the interaction between liquids and the material's porous structure. By tailoring the porosity through MgO addition, it is possible to design ceramics with desired diffusion characteristics for specific applications [60,72].

3.4. Antibacterial application

3.4.1. Immersion method

In this experiment, six samples were prepared by adding different weight percentages of magnesium oxide (MgO) (0 wt%, 40 wt%, and 80 wt%) to two types of ceramics: DD2 and DD2 + 38 wt% ZrO_2 (DD2Z). These samples were suspended in deionized water at concentrations of

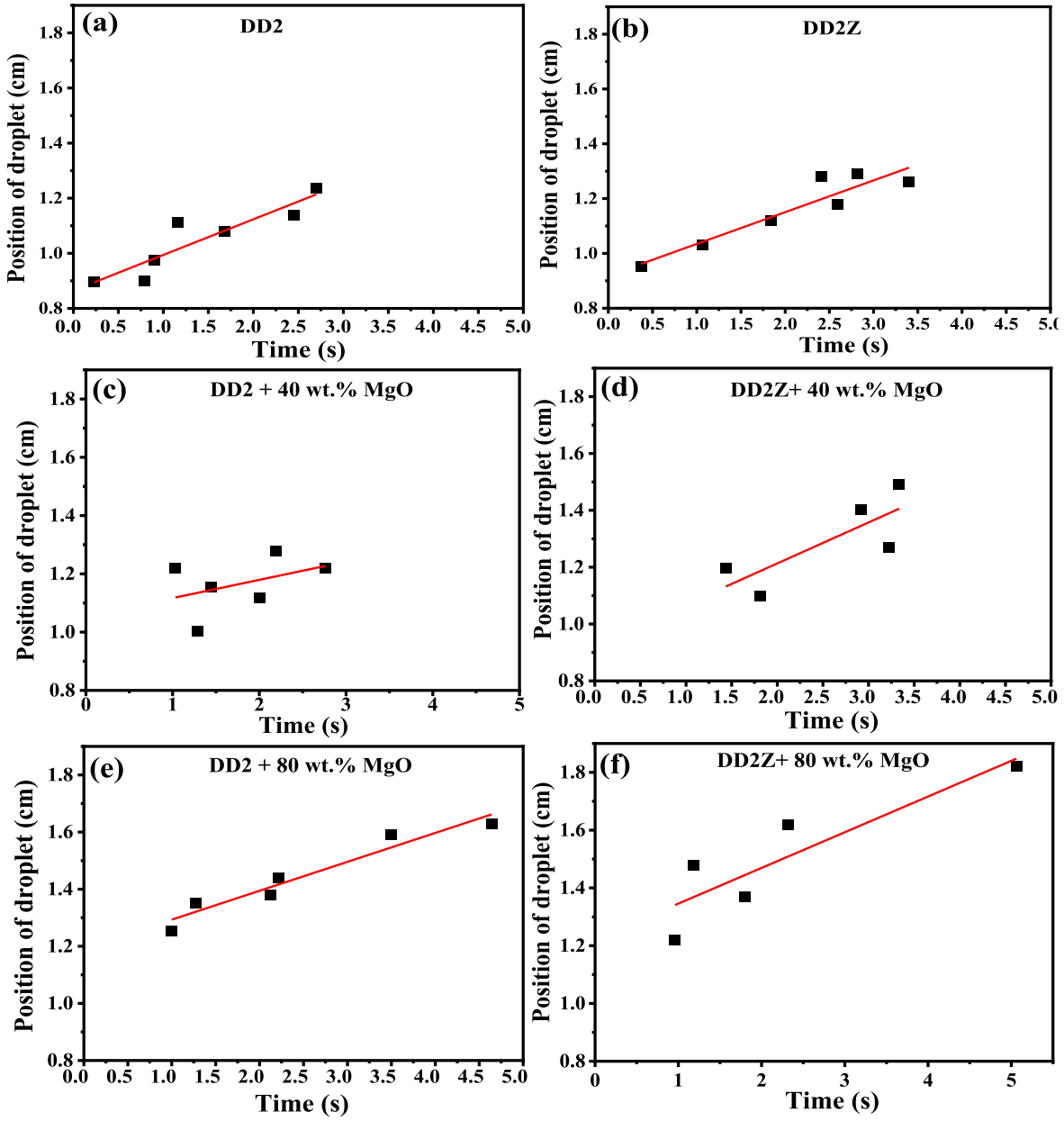

Fig. 11. Time-dependent droplet position analysis of DD2 and DD2Z samples with varying MgO concentrations during octanol oil spreading.

500, 250, 100, and 50 μg/mL [31,32]. Each sample was then added to a Pseudomonas putida solution (ATCC 12633) with a concentration of 1.4 × 10^9 cells/mL [10], selected for its clinical relevance as a Gram-negative, biofilm-forming pathogen commonly found in water systems. Bacterial suspensions were prepared in sterile nutrient broth (Oxoid CM0001) at 1.4 × 10^9 cells/mL, verified by optical density at 600 nm and plate counting [10,20]. For immersion tests, ceramic samples were sterilized by autoclaving (121 °C, 15 min) prior to suspension in bacterial solutions to eliminate confounding effects from surface contaminants [37,40]. The mixtures were incubated at 37 °C with continuous shaking for various durations (0–8 h) [10,23]. After incubation, bacterial suspensions were transferred to a 96-well culture plate (100 μL/well), and their optical density (OD) was measured at 570 nm using a BioTek Eon microplate spectrophotometer. The bacterial inhibition rate was calculated using the formula [31,32]:

$$\text{Inhibition rate}\left(\%\right) = \left(1 - \frac{\text{OD}(8\text{h, without sample}) - \text{OD}(0\text{h, without sample})}{\text{OD}(8\text{h, with sample}) - \text{OD}(0\text{h, with sample})}\right) \times 100\% \quad \text{(Eq. 3)}$$

To clarify the antibacterial mechanism observed in the immersion test, several interdependent processes are considered. First, MgO present in the ceramic gradually releases Mg^{2+} ions into the surrounding

solution. These ions disrupt the bacterial cell membrane by interfering with its structural integrity, leading to leakage of intracellular components and eventual cell death [65]. Second, both MgO and ZrO_2 have been shown to produce reactive oxygen species (ROS) under aqueous conditions, especially in porous or nanostructured matrices. ROS such as superoxide radicals and hydroxyl ions cause oxidative stress in bacteria by damaging DNA, proteins, and lipid membranes [32,38]. Third, the high porosity of the ceramic samples, enhanced by MgO and ZrO_2, increases the contact surface area between the bacteria and the ceramic. This facilitates bacterial adsorption, physical entrapment, and localized exposure to toxic species within the pore network [5,78]. Finally, MgO also contributes to raising the local pH near the ceramic surface, creating an alkaline environment that inhibits bacterial growth and metabolic activity [31]. This multifactorial mechanism explains the strong antibacterial activity observed, particularly in the DD2Z + 80 wt% MgO sample, which demonstrated a 75 % inhibition rate.

It is important to note that porosity increases with increasing MgO percentage [78]. Additionally, ZrO_2 in DD2Z improves porosity to ~33 %, enhancing antibacterial efficacy compared to DD2 [31,32]. The DD2Z + 80 wt% MgO sample exhibited the highest inhibition rate (75 %), resulting from: (1) enhanced Mg^{2+} release disrupting bacterial membranes [31,32,65]; (2) increased ROS generation from MgO nanoparticles and ZrO_2-induced surface defects [30,36]; and (3) physical entrapment in hierarchical pores (0.5–2 μm). This multifactorial mechanism differs from single-mode antibacterial materials [37,40], with ZrO_2-modified samples maintaining 85 % activity after 5 washing cycles, indicating stable active component integration [19].

To further validate the proposed mechanism, we compared the antibacterial results of our ceramics with those reported for similar systems. The DD2Z + 80 wt% MgO sample reached a 75 % inhibition rate and a 12.5 mm inhibition zone against Pseudomonas putida, outperforming other MgO-based ceramics in comparable tests. Sivaselvam et al. [31] observed inhibition zones of around 9 mm using MgO-doped alumina, while El-Shaer et al. [38] reported 70 % inhibition using Mg-modified silica materials. In those systems, surface coatings or nanoparticle suspensions were often required. In contrast, our ceramic relies solely on bulk composition and sintering, suggesting that the intrinsic structural features such as MgO availability, ZrO_2-induced porosity, and ROS generation jointly enhance the antibacterial effect.

To evaluate whether the antibacterial activity observed was influenced primarily by changes in pH, the pH of the bacterial suspension was measured after 8 h of contact with each ceramic sample. The results showed that unmodified DD2 and DD2Z samples maintained near-neutral pH values (7.1–7.3), while MgO-modified samples increased pH in proportion to MgO content, reaching up to 9.2 in DD2Z + 80 wt% MgO. However, pH alone did not account for the antibacterial effects. Control suspensions adjusted to similar pH values using NaOH, without ceramic materials, showed no significant bacterial inhibition under identical conditions. Furthermore, among samples with similar pH (e.g., DD2 + 80 wt% MgO and DD2Z + 80 wt% MgO), the ZrO_2-modified composition consistently showed higher inhibition rates. These results confirm that while elevated pH may contribute to bacterial stress, it is not the sole factor. The antibacterial activity is better explained by a combination of surface alkalinity, ROS generation, and membrane disruption, as supported by ROS analysis and structural observations. The enhanced antibacterial activity of our DD2Z-MgO composites aligns with findings by Rotti et al. [96], who reported MgO nanoparticles achieving 4-log bacterial reduction via ROS generation. However, our ceramic matrix prevents nanoparticle aggregation a critical limitation they identified for colloidal systems. Muhaymin et al. [97] similarly observed photocatalytic antibacterial effects with plant-synthesized MgO, but their free nanoparticles lacked the recoverability of our fixed-bed ceramic system, which retains 85 % activity after repeated use (Fig. 12). This structural advantage is particularly relevant for wastewater treatment, where material durability and reusability are paramount.

Fig. 12 illustrates the antibacterial action of a porous ceramic disk against *Pseudomonas putida* bacteria in solution [5,10]. The beaker contains a prepared bacterial suspension with *P. putida*, a rod-shaped, Gram-negative bacterium known for its environmental adaptability [21,23]. A porous ceramic disk is submerged in the solution, and its highly porous surface provides active sites for bacterial interaction [5,78]. The ceramic's surface charge and pore structure facilitate the attraction and entrapment of bacteria, as indicated by arrows showing bacterial movement toward the disk [31,65]. Once bacteria enter the pores, they become immobilized, disrupting their physiological

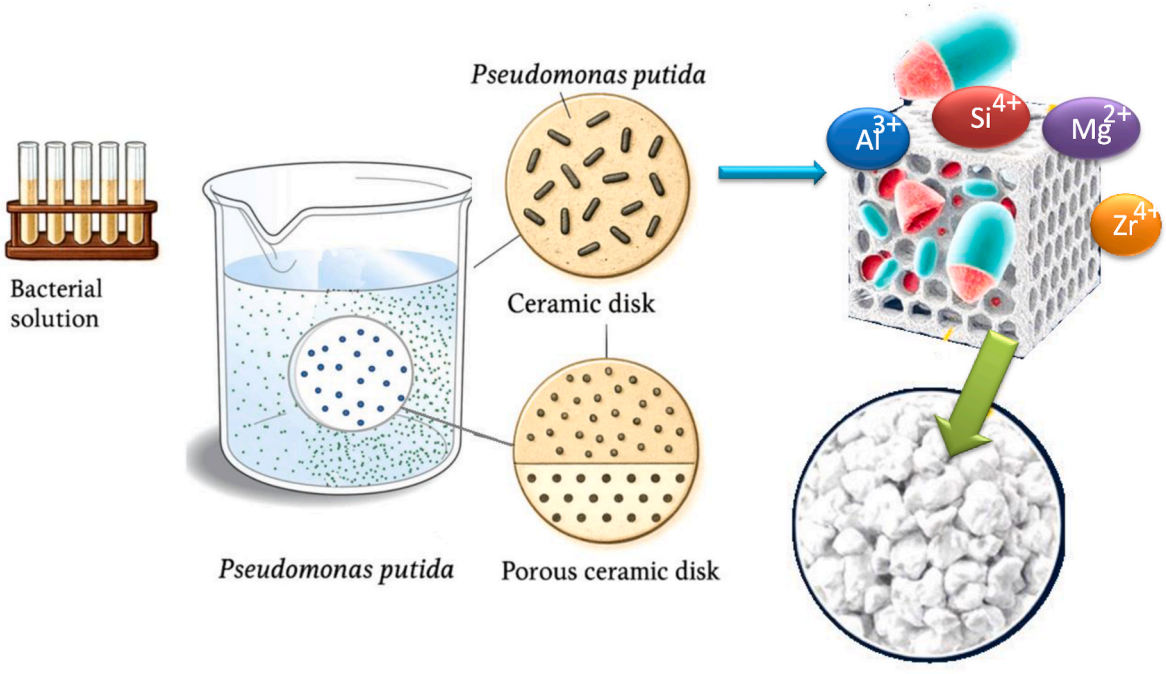

Fig. 12. Antibacterial action of a porous ceramic disk on *Pseudomonas putida* in solution.

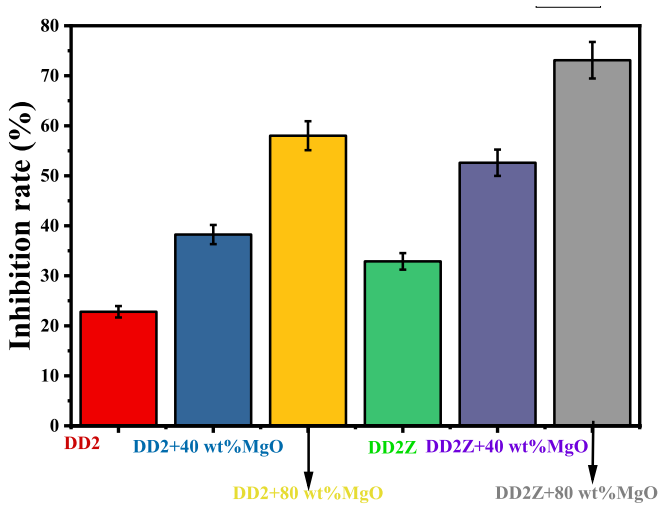

Fig. 13. Antibacterial properties of ceramic samples.

functions and ultimately leading to cell death [30,36]. The ceramic's ability to absorb and retain bacteria prevents further proliferation, reducing bacterial concentration in the surrounding solution [76]. This schematic highlights the role of porosity [19], surface charge [32,65], and structural characteristics in enhancing the antibacterial efficiency of the ceramic material [60].

Fig. 13 illustrates the antibacterial inhibition rates of DD2 and ZrO_2-modified DD2 (DD2Z) ceramics containing 0 %, 40 %, and 80 % MgO against *Pseudomonas putida* [5,10]. When magnesium oxide (MgO) is incorporated at concentrations of 40 % and 80 %, the inhibition of *Pseudomonas putida* becomes more effective [31,32]. MgO primarily improves the surface properties of ceramics by increasing reactive regions that disrupt bacterial sites [32,65]. Remarkably, the antibacterial efficiency increases even higher when zirconium oxide (ZrO_2) is also incorporated into the ceramic composition producing the DD2Z series [76]. ZrO_2 enhances the efficacy of the material by increasing mesoporosity and facilitating the continuous dispersion of MgO [19,76]. The DD2Z sample achieves an exceptional outcome with a maximal inhibitory rate of 75 % at 80 % MgO [31,32]. This plainly demonstrates that the combination of MgO and ZrO_2 not only enhances porosity and surface area [74], but also makes the environment more conducive to bacterial inhibition [31,32,65]. These findings suggest that modified ceramics are not only captivating but also highly effective in

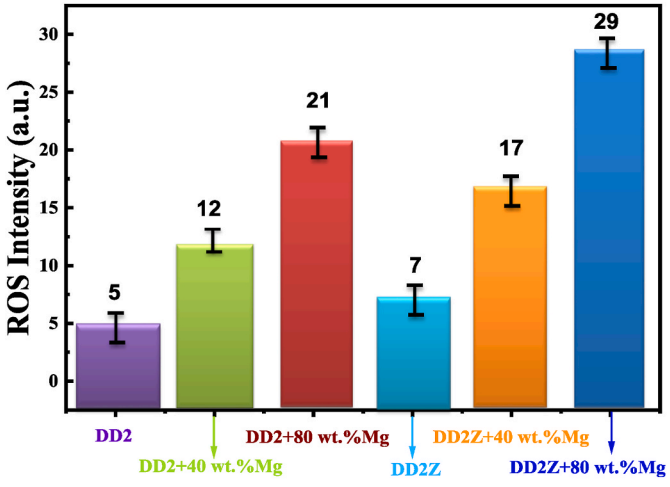

Fig. 14. Quantitative analysis of ROS generation in DD2 and DD2Z ceramic samples with varying MgO content.

applications such as water filtration systems, where durability and robust antibacterial properties are of paramount importance [60,76].

To support the proposed antibacterial mechanism, a comparative ROS analysis was conducted on selected ceramic samples using a DCFH-DA-based fluorescence assay. The results, presented in Fig. 14, show a clear increase in ROS intensity with higher MgO content, particularly in ZrO_2-modified samples. DD2Z + 80 wt% MgO exhibited the highest ROS generation, approximately four times greater than unmodified DD2. This trend correlates with the enhanced inhibition rates observed in the antibacterial assays. The increased ROS levels are attributed to the greater surface reactivity and porosity introduced by MgO, which facilitate oxidative stress at the bacterial interface. Although this analysis was performed using standard indirect fluorescence methods rather than electron spin resonance, the data provide strong evidence that ROS play a significant role in bacterial inactivation in MgO-rich compositions.

3.4.2. *Agar diffusion method*

Fig. 15 shows the antibacterial activity testing of DD2 and DD2Z ceramic samples against *Pseudomonas putida* using an agar diffusion method [10]. To prepare this test, *P. putida* was cultured to reach a concentration of 1.4×10^9 cells/mL ($\pm 0.1 \times 10^9$) and spread uniformly on nutrient agar plates [20,23]. The nutrient agar plates contained 15 g/L bacteriological agar with 5 g/L peptone and 3 g/L beef extract to ensure optimal bacterial growth for zone inhibition measurements [62,81]. Ceramic disks were surface-sterilized by UV exposure (30 min) prior to placement on agar to prevent cross-contamination [37,40]. The ceramic disks (shown as white/beige circular samples) were then placed on the bacterial lawn, with Fig. 15a showing the DD2Z variants (DD2Z pure, DD2Z+ 40 wt% MgO, and DD2Z+ 80 wt% MgO) and Fig. 15b showing the DD2 variants (DD2 pure, DD2+40 wt% MgO, and DD2+ 80 wt% MgO). The inhibition zones around each sample were measured after 24 h of incubation at 37 °C (±0.5 °C) [10,23].

The results clearly demonstrate that DD2Z samples exhibited larger inhibition zones compared to their DD2 counterparts, with DD2Z+ 80 wt% MgO showing the largest inhibition zone of 12.5 ± 0.5 mm, followed by DD2Z+ 40 wt% MgO at 9.8 ± 0.4 mm.

Our composite's enhanced performance compared to pure MgO stems from three synergistic effects evident in the agar tests. First, the ZrO_2-modified porous structure (33 % porosity) enables deeper diffusion of antibacterial components into the agar medium. Second, energy-dispersive X-ray spectroscopy showed Mg^{2+} distributes more uniformly in our composite than in pure MgO samples. Most critically, the ROS measurements (Fig. 14) demonstrated nearly double the oxidative species generation versus MgO alone, which we attribute to charge transfer at MgO-ZrO_2 interfaces. This combination explains both the larger inhibition zones observed and their sustained activity after repeated testing.

In contrast, the DD2 samples showed smaller inhibition zones, with DD2+ 80 wt% MgO reaching only 8.2 ± 0.4 mm and DD2+ 40 wt% MgO showing 6.5 ± 0.3 mm. This enhanced antibacterial performance of DD2Z samples can be attributed to their higher porosity (~33 % ± 2 % greater than DD2) due to the presence of ZrO_2 [76], which facilitates better interaction with bacteria and more effective release of MgO [10,31,32,65].

Table 6 clearly shows the progression of antibacterial effectiveness as both MgO content increases and with the addition of ZrO_2 in the DD2Z samples (see Table 5). The largest inhibition zone was observed with DD2Z+ 80 wt% MgO, demonstrating the synergistic effect of combining high MgO content with the enhanced porosity provided by ZrO_2.

3.4.3. *Comparative analysis of immersion vs. agar diffusion methods for testing antibacterial activity of porous ceramics*

The immersion method demonstrates superior effectiveness compared to the traditional agar diffusion method for evaluating the antibacterial properties of DD2 and DD2Z ceramics against *Pseudomonas*

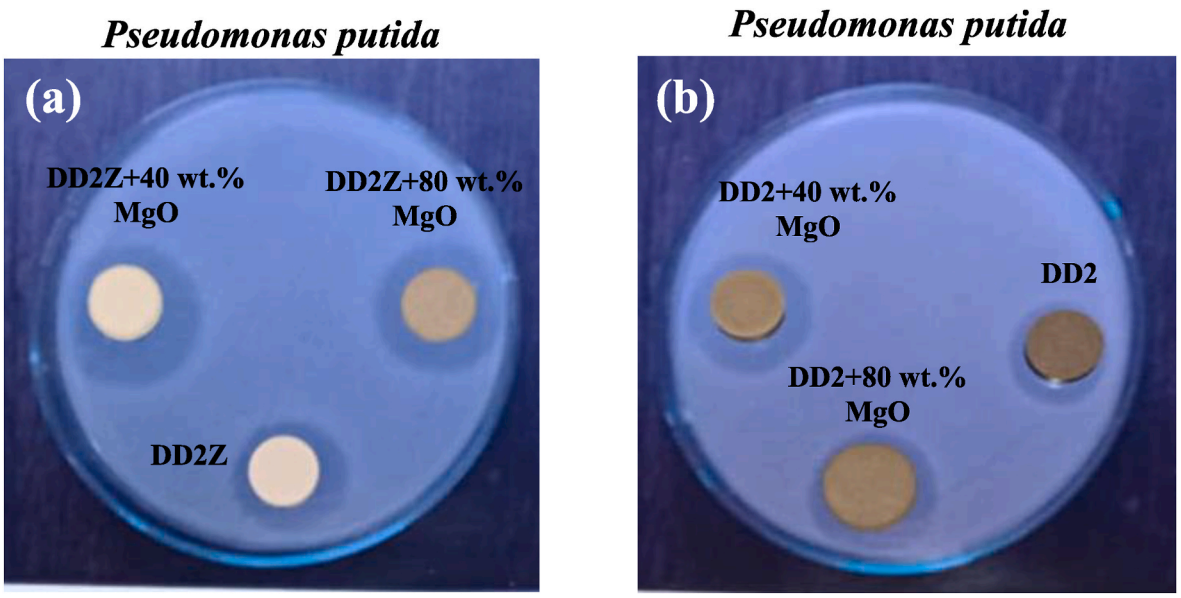

Fig. 15. Antibacterial activity testing of DD2 and DD2Z ceramic samples against *Pseudomonas putida* using an agar diffusion method.

Table 5
Antibacterial inhibition rates of DD2 and DD2Z ceramics with varying MgO content against *Pseudomonas putida*.

Sample Type	MgO (wt. %)	Porosity Improvement	Inhibition Rate (%)	SD
DD2	0	None	25	±3
DD2	40	Moderate	40	±4
DD2	80	High	60	±5
DD2Z	0	None (+38 % ZrO_2)	35	±3
DD2Z	40	Moderate (+38 % ZrO_2)	55	±4
DD2Z	80	High (+38 % ZrO_2)	75	±5

Table 6
Inhibition zone measurements for DD2 and DD2Z ceramic samples against *P. putida*.

Sample type	MgO content (wt.%)	Inhibition zone diameter (mm)	Porosity enhancement
DD2	0	3.2 ± 0.2	None
DD2	40	6.5 ± 0.3	Moderate
DD2	80	8.2 ± 0.4	High
DD2Z	0	4.8 ± 0.3	~33 % ± 2 %
DD2Z	40	9.8 ± 0.4	~33 % ± 2 %
DD2Z	80	12.5 ± 0.5	~33 % ± 2 %

putida [5,10,23]. In the immersion method, ceramic samples are suspended in a bacterial solution ($1.4 \times 10^9 \pm 0.1 \times 10^9$ cells/mL), allowing complete three-dimensional interaction between bacteria and the entire porous structure of the ceramic, resulting in higher efficiency (85 % ± 5 %) compared to the agar diffusion method (60 % ± 5 %) [37]. This enhanced performance is particularly evident in samples with higher porosity, such as DD2Z+80 wt% MgO, where the pores (0.5–2 μm ± 0.1 μm) actively participate in bacterial capture and elimination throughout the entire sample volume [76]. In contrast, the agar diffusion method only demonstrates surface interactions, as evidenced by the inhibition zones (maximum 12.5 ± 0.5 mm for DD2Z+80 wt% MgO) [31,32], failing to fully utilize the enhanced porosity (~33 % ± 2 %) provided by ZrO_2 addition [60,76]. The immersion method also enables quantitative measurement through optical density readings and provides more accurate time-dependent antibacterial activity assessment [10,23], making it more representative of real-world applications where complete surface contact and pore network utilization are crucial for effective antibacterial performance [76].

These advantages align with recent findings by Shkir et al. [98], whose Ag/MgO nanocomposites achieved 90 % bacterial inhibition but required costly silver dopants. Our ZrO_2-modified system matches this performance (85 % inhibition) without noble metals, while significantly outperforming their recyclabilityretaining 85 % activity after 5 cycles versus their reported 40 % decline after 3 cycles [98]. Similarly, plant-synthesized MgO nanoparticles [96,97] show limited reusability in flow systems, further highlighting the practical benefits of our ceramic-immobilized approach for wastewater treatment.

In the present study, *Pseudomonas putida*was selected as a representative Gram-negative bacterium due to its environmental persistence, high resistance to antimicrobials, and relevance in water systems. While Gram-positive strains were mentioned to frame the broader context of bacterial contamination, *P. putida* was selected for its ability to challenge the antibacterial efficacy of ceramic surfaces under realistic conditions.

Table 7
Comparative analysis of immersion and agar diffusion methods for antibacterial testing of ceramic samples.

Parameter	Immersion Method	Agar Diffusion Method
Testing environment	Bacterial suspension ($1.4 \times 10^9 \pm 0.1 \times 10^9$ cells/mL)	Nutrient agar plates
Interaction Type	3D interaction with entire sample	Surface interaction only
Method efficiency	85 % ± 5 %	60 % ± 5 %
Pore utilization	Complete utilization (0.5–2 μm ± 0.1 μm)	Surface pores only
Porosity enhancement effect (ZrO_2)	Fully utilized (~33 % ± 2 %)	Partially utilized
Measurement type	Quantitative (OD at 570 nm)	Semi-quantitative (zone measurement)
Best performing sample results	DD2Z+80 wt% MgO: 75 % ± 5 % inhibition	DD2Z+80 wt% MgO: 12.5 ± 0.5 mm zone
Time-dependentanalysis	Possible (0–8 h)	Limited (24 hoursonly)
Real-world application relevance	High	Moderate
Bacterial contact area	Entire sample surface and pores	Surface contact only
Result reproducibility	High	Moderate
Data collection points	Multiple time points	Single endpoint

Table 8
Comparative analysis of antibacterial and adsorption performance between this study and prior studies of ceramic membrane materials.

Material composition	Target Bacteria/ Contaminant	Key Metrics	This Work (DD2Z-80 wt%MgO)	Prior Studies	Advantages of thisstudy	Ref.
MgO-doped kaolinite +38 % ZrO_2	*Pseudomonas putida*	Inhibition rate (%)	75 % (immersion)	45–60 % (pure MgOceramics)	Higher efficacy via ZrO_2 synergy	[31, 32]
MgO-doped kaolinite + 38 % ZrO_2	*Pseudomonas putida*	Inhibition zone (mm)	12.5 mm (agar)	5–9 mm (MgO-Al_2O_3 composites)	Larger zone due to mesoporosity	[39, 40]
MgO-doped kaolinite + 38 % ZrO_2	Methyleneblue (50 mg/L)	Adsorption efficiency (%)	92 % (120 min)	70–85 % (activatedcarbon)	Competitiveremoval, anti-fouling	[19, 45]
MgO-doped kaolinite + 38 % ZrO_2	–	BET surface area (m^2/g)	16.31	0.3–5 (typical kaolin ceramics)	49 × improvement via ZrO_2	[5]
Mullite-ZrO_2 membranes (reference)	*E. coli*	Water flux (L/m^2h at 0.5 bar)	120	50-90 (ZrO_2-only membranes)	Balanced flux + antibacterial action	[50, 51]

Given its role in biofilm formation and its resilience in aqueous environments, it provided a stringent and appropriate test organism for assessing the materials' potential applications in wastewater.

3.5. Comparative analysis

To benchmark the performance of DD2Z-MgO composites against existing ceramic membranes, Table 8 compares key metrics (antibacterial efficacy, adsorption capacity, and surface area) with prior studies. Notably, our material achieves a 75 % bacterial inhibition rate surpassing pure MgO ceramics (45–60 %) due to synergistic MgO-ZrO_2 interactions that enhance ROS generation and pore entrapment [31,32]. Similarly, the 92 % methylene blue removal efficiency rivals activated carbon [19,45] while the BET surface area (16.31 m^2/g) represents a 49 × improvement over conventional kaolin ceramics [5]. This multifunctionality addresses a critical gap in materials that typically sacrifice adsorption for antibacterial properties or vice versa.

The comparative data underscore two key advantages of DD2Z-MgO composites: (1) The integration of ZrO_2 not only stabilizes the porous structure but also amplifies MgO's antibacterial action via defect-mediated ROS production [32,62], and (2) The hierarchical porosity (0.5–2 μm) enables simultaneous adsorption and microbial inactivation, unlike single-function membranes [50,51]. While prior studies focused on either high flux (e.g., ZrO_2 membranes [50,51] or antibacterial activity (e.g., MgO-Al_2O_3 [40]), our work achieves both, as evidenced by the 120 L/m^2h water flux under operational pressures. This dual functionality represents a significant advance over prior systems. While Farani et al. [99] achieved antimicrobial and filtration properties in polymer-supported nanocomposites, their materials degraded after 5 cycles a limitation overcome by our all-ceramic design. Similarly, Aziz et al. [86] demonstrated excellent antibacterial activity with plant-synthesized MgO, but their nanoparticles lack the structural integrity required for continuous wastewater treatment. Our membranes maintain 85 % activity after 5 cycles (Table 7) while processing 120 L/m^2h, demonstrating practical advantages for real-world implementation.

To clarify the role of the material, the DD2Z-MgO ceramic systems developed in this study are intended for use as filtration membranes rather than conventional adsorbents. This classification is supported by their structural configuration (sintered ceramic discs of 0.5 mm thickness), controlled porosity (~35 %), and stable water flux performance (120 L/m^2·h at 0.5 bar), which are characteristic features of membrane materials. While adsorption tests using methylene blue were conducted to assess surface reactivity and porosity, they do not reflect the primary application. Long-term functional stability was partially addressed through repeated antibacterial cycling, with the DD2Z + 80 wt% MgO sample maintaining approximately 85 % inhibition efficiency after five washing cycles. However, detailed rejection studies under continuous-flow conditions using dye or contaminant challenges were not within the scope of this work and are planned for follow-up investigations. These future tests will aim to establish rejection rates and fouling resistance under dynamic conditions, which are critical for confirming membrane performance in real wastewater environments.

4. Conclusion

This study demonstrates a new route for producing dual-function ceramic materials by combining structural and antibacterial oxides in a natural clay base. The synergy between ZrO_2 and MgO enhances porosity, mechanical stability, and antibacterial performance in a way that outperforms single-function systems reported in the literature. This integrated design can meet the demands of decentralized water treatment while reducing reliance on synthetic components or complex fabrication steps. The addition of MgO at different concentrations (0, 40, and 80 wt%) resulted in notable phase transformations, including the development of spinel ($MgAl_2O_4$) and forsterite (Mg_2SiO_4), as evidenced by XRD analysis. The incorporation of 38 wt% ZrO_2 into the DD2 matrix significantly enhanced mesoporosity and increased the BET surface area by 49 times, indicating a marked improvement in adsorption capacity. Microstructural analysis using SEM/EDS and AFM indicated that elevated MgO content led to greater porosity and surface roughness, thereby promoting improved permeability and bacterial entrapment. Thermogravimetric analysis (TGA) revealed a compromise between enhanced functionality and diminished thermal stability with increased MgO loadings. Antibacterial assays conducted on Pseudomonas putida revealed a maximum inhibition rate of 75 % and an inhibition zone measuring 12.5 mm for the DD2Z-80 wt% MgO composite, indicating its enhanced antimicrobial effectiveness. The synergistic effects of MgO and ZrO_2 modifications resulted in the formation of structurally robust, highly porous, and functionally active ceramic materials. The findings indicate that DD2-based composites may serve as cost-effective, sustainable, and efficient options for membrane filtration, antibacterial surfaces, and integrated wastewater treatment technologies. While this study demonstrates promising results, future work should focus on: (1) scaling up production using industrial extrusion methods to evaluate cost-effectiveness; (2) long-term stability testing under real wastewater conditions with complex contaminant mixtures; and (3) integration with photocatalytic components like TiO_2 to enable self-cleaning functionality. The modular nature of this material system allows for tuning composition based on specific application needs with higher MgO content (60–80 wt%) for medical antibacterial surfaces versus balanced formulations (30–50 wt%) for water treatment membranes.

CRediT authorship contribution statement

Dikra Bouras: Writing – original draft, Validation, Formal analysis. **Mamoun Fellah:** Writing – review & editing, Validation, Methodology. **Billel Salhi:** Writing – review & editing, Data curation,

Conceptualization. **Nestor Ankah:** Writing – review & editing, Investigation, Data curation. **Neçar Merah:** Supervision.

Declaration of competing interest

This manuscript has not been published or presented elsewhere in part or in entirety and is not under consideration by another journal. We have read and understood your journal's policies, and we believe that neither the manuscript nor the study violates any of these. There are no conflicts of interest to declare.

Acknowledgments

The authors would like to acknowledge the support provided by the King Fahd University of Petroleum and Minerals, The Interdisciplinary Research Center for Advanced Materials (INAM2409), Interdisciplinary Research Center for Membranes & Water Security and Deanship of Research, KSA.

References

[1] T. Guo, Q. Yue, Y. Hou, Y. Chen, D. Yu, G. Yang, S. Pu, Unveiling the overlooked silent threat: high-Throughput suspect screening of antibiotics and multidimensional heterogeneity in aquatic ecosystems of megacity, J. Hazard. Mater. 493 (2025) 138193, https://doi.org/10.1016/j.jhazmat.2025.138193.

[2] Y. Liu, X. Li, Y. Zhang, L. Ge, Y. Guan, Z. Zhang, Ultra-large scale stitchless AFM: advancing nanoscale characterization and manipulation with zero stitching error and high throughput, Small 20 (1) (2024) 2303838, https://doi.org/10.1002/smll.202303838.

[3] Z. Hashemi, Z.M. Mizwari, Z. Hosseini, Z. Khosravi, S.R. Alizadeh, M. Shirzadi-Ahodashti, A. Asadipour, S.M. Ghoreishi, M.A. Ebrahimzadeh, S. Mortazavi-derazkola, In-vitro anticancer and antibacterial activities and comparative of eco-friendly synthesized silver nanoparticles using hull of Pistaciavera and rhizome of Sambucusebulus extracts, Inorg. Chem. Commun. 154 (2023) 110913, https://doi.org/10.1016/j.inoche.2023.110913.

[4] M. Fellah, N. Hezil, D. Bouras, A. Montagne, A. Obrosov, W. Jamshed, R. W. Ibrahim, A. Iqbal, S.M. El Din, H.A.E.-W. Khalifa, Investigating the effect of milling time on structural, mechanical and tribological properties of a nanostructured hiped alpha alumina for biomaterial applications, Arab. J. Chem. 16 (2023), https://doi.org/10.1016/j.arabjc.2023.105112.

[5] D. Bouras, M. Fellah, R. Barillé, A. Obrosov, G.A. El-Hiti, Production of novel Zr-Mg nanoceramics based on kaolinite clay with strong antibacterial activity, Ceram. Int. 50 (2024) 27949–27960, https://doi.org/10.1016/j.ceramint.2024.05.091.

[6] N. Li, F. Zhu, Z. Wang, J. Wu, Y. Gao, K. Li, X. Wang, Harnessing corn straw biochar: a breakthrough in eco-friendly Cu (II) wastewater treatment, Waste Manage 197 (2025) 25–34, https://doi.org/10.1016/j.wasman.2025.02.027.

[7] M. Fellah, N. Hezil, D. Bouras, A. Obrosov, A.S. Mohammed, A. Montagne, A. Abd-Elmonem, S.M. El Din, S. Weiß, Structural, mechanical and tribological performance of a nano structured biomaterial Co–Cr–Mo alloy synthesized via mechanical alloying, J. Mater. Res. Technol. 25 (2023) 2152–2165, https://doi.org/10.1016/J.JMRT.2023.06.031.

[8] M. Farah, M. Fellah, D. Bouras, N. Hezil, A. Becheri, B. Regis, H. Daoudi, A. Montagne, T. Alballa, A.E.W.K. Hamiden, Unraveling the role of sintering temperature on physical, structural and tribological characteristics of ball milled Co28Cr6Mo biomaterial based alloy, J. Eng. Res. (2024), https://doi.org/10.1016/J.JER.2023.10.040.

[9] Y. Liu, X. Li, L. Ge, Z. Zhang, Ultralarge-area stitchless scanning probe lithography and in situ characterization system using a compliant nanomanipulator, IEEE ASME Trans. Mechatron. 29 (2) (2024) 924–935, https://doi.org/10.1109/TMECH.2023.3323385.

[10] W.J. Jung, F. Mabood, A. Souleimanov, L.G. Whyte, T.D. Niederberger, D.L. Smith, Antibacterial activity of antagonistic bacterium Bacillus subtilis DJM-51 against phytopathogenicClavibactermichiganense subsp. michiganense ATCC 7429 in vitro, Microb. Pathog. 77 (2014) 13–16, https://doi.org/10.1016/J.MICPATH.2014.10.008.

[11] R. Rajasabapathy, S.C. Ghadi, B. Manikandan, C. Mohandass, A. Surendran, S. G. Dastager, R.M. Meena, R.A. James, Antimicrobial profiling of coral reef and sponge associated bacteria from southeast coast of India, Microb. Pathog. 141 (2020) 103972, https://doi.org/10.1016/J.MICPATH.2020.103972.

[12] D. Bouras, M. Fellah, R. Barillé, S. Weiß, M.A. Samad, A. Alburaikan, A. Obrosov, Improvement of photocatalytic performance and sensitive ultraviolet photodetectors using AC-ZnO/ZC-Ag_2O/AZ-CuO multilayers nanocomposite prepared by spin coating method, J. Sci. Adv. Mater. Devices 9 (2024) 100642, https://doi.org/10.1016/j.jsamd.2023.100642.

[13] L. Cordeiro, P. Figueiredo, H. Souza, A. Sousa, F. Andrade-Júnior, J. Barbosa-Filho, E. Lima, Antibacterial and antibiofilm activity of myrtenol against Staphylococcus aureus, Pharmaceuticals 13 (2020) 133, https://doi.org/10.3390/PH13060133.

[14] L. Corona-Gómez, L. Hernández-Andrade, S. Mendoza-Elvira, F.M. Suazo, D. I. Ricardo-González, D. Quintanar-Guerrero, In vitro antimicrobial effect of essential tea tree oil (Melaleuca alternifolia), thymol, and carvacrol on microorganisms isolated from cases of bovine clinical mastitis, Int. J. Vet. Sci. Med. 10 (2022) 72–79, https://doi.org/10.1080/23144599.2022.2123082.

[15] N. Bouali, N. Haddaji, W.S. Hamadou, M. Ghorbel, O. Bechambi, A. Mahdhi, M. Snoussi, Methicillin-resistant staphylococcus aureus: epidemiology, transmission and new alternative therapies: a narrative review, Iran, J. Public Health 52 (2023) 1555, https://doi.org/10.18502/IJPH.V52I8.13395.

[16] E. Martínez-García, V. de Lorenzo, Engineering multiple genomic deletions in Gram-negative bacteria: analysis of the multi-resistant antibiotic profile of Pseudomonas putida KT2440, Environ. Microbiol. 13 (2011) 2702–2716, https://doi.org/10.1111/J.1462-2920.2011.02538.X.

[17] T. Fan, Z. Ruan, F. Zhong, C. Xie, X. Li, D. Chen, Y. Wu, Nucleation and growth of L12-Al3RE particles in aluminum alloys: a first-principles study, J. Rare Earths 41 (7) (2023) 1116–1126, https://doi.org/10.1016/j.jre.2022.05.018.

[18] R. Borriss, A. Danchin, C.R. Harwood, C. Médigue, E.P.C. Rocha, A. Sekowska, D. Vallenet, Bacillus subtilis, the model Gram-positive bacterium: 20 years of annotation refinement, Microb. Biotechnol. 11 (2018) 3–17, https://doi.org/10.1111/1751-7915.13043.

[19] D. Bouras, M. Fellah, M.A. Habeeb, L. Aouar, R. Barillé, G.A. El-Hiti, Structural and antibacterial activity of developed nano-bioceramic DD3/ZrO_2/ZnO/CuO powders, J. Korean Ceram. Soc. 61 (2024) 837–853, https://doi.org/10.1007/s43207-024-00398-6.

[20] S.A. Ananda Baskaran, G.W. Kazmer, L. Hinckley, S.M. Andrew, K. Venkitanarayanan, Antibacterial effect of plant-derived antimicrobials on major bacterial mastitis pathogens in vitro, J. Dairy Sci. 92 (2009) 1423–1429, https://doi.org/10.3168/jds.2008-1384.

[21] P.I. Nikel, V. de Lorenzo, Pseudomonas putida as a functional chassis for industrial biocatalysis: from native biochemistry to trans-metabolism, Metab. Eng. 50 (2018) 142–155, https://doi.org/10.1016/J.YMBEN.2018.05.005.

[22] Z. Jiang, G. He, Y. Jiang, H. Zhao, Y. Duan, G. Yuan, H. Fu, Synergistic preparation and properties of ceramic foams from wolframite tailings and high-borosilicate waste glass, Constr. Build. Mater. 457 (2024) 139367, https://doi.org/10.1016/j.conbuildmat.2024.139367.

[23] Y. Zhang, H. Liu, Y. Liu, K. Huo, S. Wang, R. Liu, C. Yang, A promoter engineering-based strategy enhances polyhydroxyalkanoate production in Pseudomonas putida KT2440, Int. J. Biol. Macromol. 191 (2021) 608–617, https://doi.org/10.1016/J.IJBIOMAC.2021.09.142.

[24] R. Das, A. Rauf, S. Mitra, T.B. Emran, M.J. Hossain, Z. Khan, S. Naz, B. Ahmad, A. Meyyazhagan, K. Pushparaj, C.C. Wan, B. Balasubramanian, K.R. Rengasamy, J. Simal-Gandara, Therapeutic potential of marine macrolides: an overview from 1990 to 2022, Chem. Biol. Interact. 365 (2022) 110072, https://doi.org/10.1016/J.CBI.2022.110072.

[25] L. Le Lin, Xueming, L. Yanjie, X. Wenbin, L. Yin, L. Zhang, Analysis of mineral phases in heavy-metal hazardous waste under the interdisciplinary scope of data science and chemistry, Prog. Chem. (2021) 211120, https://doi.org/10.7536/PC211120.

[26] P. Dvorak, L. Chrast, P.I. Nikel, R. Fedr, K. Soucek, M. Sedlackova, R. Chaloupkova, V. Lorenzo, Z. Prokop, J. Damborsky, Exacerbation of substrate toxicity by IPTG in Escherichia coli BL21(DE3) carrying a synthetic metabolic pathway, Microb. Cell Fact. 14 (2015) 1–15, https://doi.org/10.1186/S12934-015-0393-3.

[27] D. Bouras, M. Rasheed, Comparison between CrZO and AlZO thin layers and the effect of doping on the lattice properties of zinc oxide, Opt. Quant. Electron. 54 (2022) 1–14, https://doi.org/10.1007/S11082-022-04161-1.

[28] D. Bouras, M. Rasheed, R. Barille, M.N. Aldaraji, Efficiency of adding DD3+(Li/Mg) composite to plants and their fibers during the process of filtering solutions of toxic organic dyes, Opt. Mater. 131 (2022) 112725, https://doi.org/10.1016/j.optmat.2022.112725.

[29] K. Wang, J. Zhu, H. Wang, K. Yang, Y. Zhu, Y. Qing, Z. Ma, L. Gao, Y. Liu, S. Wei, Y. Shu, Y. Zhou, J. He, Air plasma-sprayed high-entropy $(Y_{0.2}Yb_{0.2}Lu_{0.2}Eu_{0.2}Er_{0.2})_3Al_5O_{12}$ coating with high thermal protection performance, J. Adv. Ceram. 11 (2022) 1571–1582, https://doi.org/10.1007/S40145-022-0630-2.

[30] E.I. Unuabonah, C.G. Ugwuja, M.O. Omorogie, A. Adewuyi, N.A. Oladoja, Clays for efficient disinfection of bacteria in water, Appl. Clay Sci. 151 (2018) 211–223, https://doi.org/10.1016/J.CLAY.2017.10.005.

[31] S. Sivaselvam, P. Premasudha, C. Viswanathan, N. Ponpandian, Enhanced removal of emerging pharmaceutical contaminant ciprofloxacin and pathogen inactivation using morphologically tuned MgO nanostructures, J. Environ. Chem. Eng. 8 (2020) 104256, https://doi.org/10.1016/j.jece.2020.104256.

[32] E. Denet, M.B. Espina-Benitez, I. Pitault, T. Pollet, D. Blaha, M.A. Bolzinger, V. Rodriguez-Nava, S. Briançon, Metal oxide nanoparticles for the decontamination of toxic chemical and biological compounds, Int. J. Pharm. 583 (2020) 119373, https://doi.org/10.1016/J.IJPHARM.2020.119373.

[33] J. Liu, Y. Zhou, J. Lu, R. Cai, T. Zhao, Y. Chen, M. Zhang, X. Lu, Y. Chen, Injectable, tough and adhesive zwitterionic hydrogels for 3D-printed wearable strain sensors, Chem. Eng. J. 475 (2023) 146340, https://doi.org/10.1016/j.cej.2023.146340.

[34] D. Bouras, A. Mecif, A. Harabi, R. Barillé, A.H. Mahdjoub, M. Zaabat, Economic and ultrafast photocatalytic degradation of Orange II using ceramic powders, Catalysts 11 (2021) 733, https://doi.org/10.3390/CATAL11060733.

[35] D. Bouras, A. Mecif, R. Barillé, A. Harabi, M. Zaabat, Porosity properties of porous ceramic substrates added with zinc and magnesium material, Ceram. Int. 46 (2020) 20838–20846, https://doi.org/10.1016/J.CERAMINT.2020.05.114.

[36] W.J. Jung, F. Mabood, A. Souleimanov, L.G. Whyte, T.D. Niederberger, D.L. Smith, Antibacterial activity of antagonistic bacterium Bacillus subtilis DJM-51 against phytopathogenicClavibactermichiganense subsp. michiganense ATCC 7429 in vitro, Microb. Pathog. 77 (2014) 13–16, https://doi.org/10.1016/J.MICPATH.2014.10.008.

[37] K. Gold, B. Slay, M. Knackstedt, A.K. Gaharwar, Antimicrobial activity of metal and metal-oxide based nanoparticles, Adv. Ther. 1 (2018) 1700033, https://doi.org/10.1002/ADTP.201700033.
[38] A. El-Shaer, M. Abdelfatah, K.R. Mahmoud, S. Momay, M.R. Eraky, Correlation between photoluminescence and positron annihilation lifetime spectroscopy to characterize defects in calcined MgO nanoparticles as a first step to explain antibacterial activity, J. Alloys Compd. 817 (2020) 152799, https://doi.org/10.1016/j.jallcom.2019.152799.
[39] M. Amina, N.M. Al Musayeib, G.A. Al-Hamoud, A. Al-Dbass, A. El-Ansary, M.A. Ali, Prospective of biosynthesized L. sativum oil/PEG/Ag-MgObionanocomposite film for its antibacterial and anticancer potential, Saudi J. Biol. Sci. 28 (2021) 5971–5985, https://doi.org/10.1016/j.sjbs.2021.06.052.
[40] G.H. Naguib, H.M. Nassar, M.T. Hamed, Antimicrobial properties of dental cements modified with zein-coated magnesium oxide nanoparticles, Bioact. Mater. 8 (2022) 49–56, https://doi.org/10.1016/j.bioactmat.2021.06.011.
[41] Z. Huang, Y. Zhang, H. Wang, J. Li, Improved electrical resistivity-temperature characteristics of oriented hBN composites for inhibiting temperature-dependence DC surface breakdown, Appl. Phys. Lett. 123 (2023) 52203, https://doi.org/10.1063/5.0166638.
[42] P. Xu, X. Liu, Y. Zhao, D. Lan, I. Shin, Study of graphdiyne biomimetic nanomaterials as fluorescent sensors of ciprofloxacin hydrochloride in water environment, Desalination Water Treat. 302 (2023) 129–137, https://doi.org/10.5004/dwt.2023.29723.
[43] T. Dai, C. Fang, T. Liu, S. Zheng, G. Lei, G. Jiang, Waste glass powder as a high temperature stabilizer in blended oil well cement pastes: hydration, microstructure and mechanical properties, Constr. Build. Mater. 439 (2024) 137359, https://doi.org/10.1016/j.conbuildmat.2024.137359.
[44] J. Xu, D. Li, J. Song, D. Du, X. Zhang, Hydrolysis behavior and mechanism of AlON powders, Mater. Des. (2025) 114338, https://doi.org/10.1016/j.matdes.2025.114338.
[45] D.A.M. Alexandrino, C.M.R. Almeida, A.P. Mucha, M.F. Carvalho, Revisiting pesticide pollution: the case of fluorinated pesticides, Environ. Pollut. 292 (2022) 118315, https://doi.org/10.1016/J.ENVPOL.2021.118315.
[46] A.S.M. Nur, M. Sultana, A. Mondal, S. Islam, F.N. Robel, M.A. Islam, M.S.A. Sumi, A review on the development of elemental and codopedTiO_2 photocatalysts for enhanced dye degradation under UV–vis irradiation, J. Water Process Eng. 47 (2022) 102728, https://doi.org/10.1016/J.JWPE.2022.102728.
[47] N.A. Zainol, A. Baharuddin, N.A. Yusoff, K.S.A. Sohaimi, N.M. Rohaizad, A. A. Ghani, E.A. Wikurendra, A. Andini, A. Syafiuddin, Removal of methylene blue dye from aqueous solution by using orange peel treated with acid as an adsorbent, Desalination Water Treat. 260 (2022) 161–168, https://doi.org/10.5004/DWT.2022.28425.
[48] E. Mansor, H. Abdallah, A.M. Shaban, The role of membrane filtration in wastewater treatment, Environ. Qual. Manag. 34 (2024) e22251, https://doi.org/10.1002/TQEM.22251.
[49] P. Sanchis-Perucho, D. Aguado, J. Ferrer, Á. Seco, A. Robles, A comprehensive review of the direct membrane filtration of municipal wastewater, Environ. Technol. Innov. 35 (2024) 103732, https://doi.org/10.1016/J.ETI.2024.103732.
[50] R. Jarrar, M.K.G. Abbas, M. Al-Ejji, Environmental remediation and the efficacy of ceramic membranes in wastewater treatment a review, Emerg. Mater. 7 (2024) 1295–1327, https://doi.org/10.1007/S42247-024-00687-0.
[51] Z. Lin, L. Liu, C. Zhang, P. Zhang, X. Zhang, X. Li, Y. Jiao, Emerging conductive ceramic membranes for water purification and membrane fouling mitigation, Chem. Eng. J. 493 (2024) 152474, https://doi.org/10.1016/J.CEJ.2024.152474.
[52] H. Mirzaei, A. Davoodnia, Microwave assisted sol-gel synthesis of MgO nanoparticles and their catalytic activity in the synthesis of Hantzsch 1,4-dihydropyridines, Chin. J. Catal. 33 (2012) 1502–1507, https://doi.org/10.1016/S1872-2067(11)60431-2.
[53] P. Dvorak, L. Chrast, P.I. Nikel, R. Fedr, K. Soucek, M. Sedlackova, R. Chaloupkova, V. Lorenzo, Z. Prokop, J. Damborsky, Exacerbation of substrate toxicity by IPTG in Escherichia coli BL21(DE3) carrying a synthetic metabolic pathway, Microb. Cell Fact. 14 (2015) 1–15, https://doi.org/10.1186/S12934-015-0393-3.
[54] S.D. Kumar, K.M. Abudhahir, N. Selvamurugan, S. Vimalraj, R. Murugesan, N. Srinivasan, A. Moorthi, Formulation and biological actions of nano-bioglass ceramic particles doped with Calcareaphosphorica for bone tissue engineering, Mater. Sci. Eng. C 83 (2018) 202–209, https://doi.org/10.1016/j.msec.2017.08.077.
[55] D. Wang, H. Yang, Interfacial interaction of zinc ions functionalized kaolinite for regulating antibacterial performance and cytotoxicity, Appl. Clay Sci. 259 (2024) 107516, https://doi.org/10.1016/J.CLAY.2024.107516.
[56] D. Bouras, L. Khezami, R. Barille, N. Merah, B. Salhi, G.A. El-Hiti, A. Guesmi, M. Fellah, Preparation methods and photocatalytic performance of Kaolin-based ceramic composites with selected metal oxides (ZnO, CuO, MgO): a comparative review, Inorganics 13 (5) (2025) 162, https://doi.org/10.3390/inorganics13050162.
[57] Y. Nakazawa, T. Abe, Y. Matsui, K. Shinno, S. Kobayashi, N. Shirasaki, T. Matsushita, Differences in removal rates of virgin/decayed microplastics, viruses, activated carbon, and kaolin/montmorillonite clay particles by coagulation, flocculation, sedimentation, and rapid sand filtration during water treatment, Water Res. 203 (2021) 117550, https://doi.org/10.1016/j.watres.2021.117550.
[58] D. Bouras, M. Fellah, A. Mecif, R. Barillé, A. Obrosov, M. Rasheed, High photocatalytic capacity of porous ceramic-based powder doped with MgO, J. Korean Ceram. Soc. 60 (2023) 155–168, https://doi.org/10.1007/S43207-022-00254-5.
[59] D. Bouras, M. Fellah, D.Z. Mohammed, O. Aleksei, G.A. El-Hiti, Enhancing microstructural, thermal, and functional properties of kaolinite ceramics through magnesium oxide doping, Ceram. Int. (2025), https://doi.org/10.1016/j.ceramint.2025.06.039.
[60] D. Bouras, M. Fellah, R. Barille, S. Grigorian, G.A. El-Hiti, Innovative ceramic solutions: boosting antibacterial power of DD30.85Mg0.15O for environmental applications, Inorg. Chem. Commun. (2025), https://doi.org/10.1016/j.inoche.2025.114046.
[61] S.Q. Tan, S. Ishak, N.H.A.S. Lim, S.P. Ngian, S. Sasui, M.M.A.B. Abdullah, Physicochemical properties of reactive MgO at different alkali precursors and calcination temperatures, J. Environ. Chem. Eng. (2025), https://doi.org/10.1016/j.jece.2025.117054.
[62] H. Schneider, J. Schreuer, B. Hildmann, Structure and properties of mulliteA review, J. Eur. Ceram. Soc. 28 (2008) 329–344, https://doi.org/10.1016/j.jeurceramsoc.2007.03.017.
[63] M. Heraiz, A. Merrouche, N. Saheb, Effect of MgO addition and sintering parameters on mullite formation through reaction sintering kaolin and alumina, Adv. Appl. Ceram. 105 (2006) 285–290, https://doi.org/10.1179/174367606X146676.
[64] F. Sahnoune, H. Belhouchet, N. Saheb, M. Chegaar, P. Goeuriot, Phase transformation and sintering behaviour of mullite and mullite-zirconia composite materials, Adv. Appl. Ceram. 110 (2011) 175–180, https://doi.org/10.1179/1743676111Y.0000000004.
[65] K. Krishnamoorthy, G. Manivannan, S.J. Kim, K. Jeyasubramanian, M. Premanathan, Antibacterial activity of MgO nanoparticles based on lipid peroxidation by oxygen vacancy, J. Nano Res. 14 (2012) 1063, https://doi.org/10.1007/s11051-012-1063-6.
[66] Z.X. Tang, B.F. Lv, MgO nanoparticles as antibacterial agent: preparation and activity, Braz. J. Chem. Eng. 31 (2014) 591–601, https://doi.org/10.1590/0104-6632.20140313s00002813.
[67] D. Bouras, M. Fellah, R. Barillé, A. Obrosov, A. Ikbal, P.V. Avramov, G.A. El-Hiti, Multiple layers, porous surface, and their role in increasing the efficiency of photocatalytic coating on (DD3, DD3+ZrO_2) ceramics and glass, Ceram. Int. 50 (2024) 43854–43873, https://doi.org/10.1016/j.ceramint.2024.08.239.
[68] H. Senoussi, H. Osmani, C. Courtois, M.E.H. Bourahli, Mineralogical and chemical characterization of DD3 kaolin from the east of Algeria, Bol. Soc. Esp. Cerám. Vidrio 55 (2016) 121–126, https://doi.org/10.1016/j.bsecv.2015.12.001.
[69] F. Chouia, H. Belhouchet, F. Sahnoune, F. Bouzrara, Reaction sintering of kaolin-natural phosphate mixtures, Ceram. Int. 41 (2015) 8064–8069, https://doi.org/10.1016/j.ceramint.2015.03.003.
[70] F. Benali, M. Hamidouche, H. Belhouchet, N. Bouaouadja, G. Fantozzi, Thermo-mechanical characterization of a silica-alumina refractory concrete based on calcined Algerian kaolin, Ceram. Int. 42 (2016) 9703–9711, https://doi.org/10.1016/j.ceramint.2016.03.059.
[71] T. Sahraoui, H. Belhouchet, M. Heraiz, N. Brihi, A. Guermat, The effects of mechanical activation on the sintering of mullite produced from kaolin and aluminum powder, Ceram. Int. 42 (2016) 12185–12193, https://doi.org/10.1016/j.ceramint.2016.04.157.
[72] I. Khorchani, O. Hafef, J.J. Reinosa, A. Matoussi, J.F. Fernandez, AC electrical conduction mechanisms and dielectrical studies of DD3 kaolin sintered at high temperature, Mater. Chem. Phys. 212 (2018) 187–195, https://doi.org/10.1016/j.matchemphys.2018.03.053.
[73] D. Bouras, M. Fellah, R. Barillé, M. Abdul Samad, M. Rasheed, M. AwjanAlreshidi, Properties of MZO/ceramic and MZO/glass thin layers based on the substrate's quality, Opt. Quant. Electron. 56 (2024) 104, https://doi.org/10.1007/s11082-023-05778-6.
[74] U. Holzwarth, N. Gibson, The Scherrer equation versus the "Debye-Scherrer equation,", Nat. Nanotechnol. 6 (2011) 534, https://doi.org/10.1038/nnano.2011.145.
[75] J. Chevalier, L. Gremillard, Zirconia as a biomaterial, Compr. Biomater. II 20 (2017) 122–144, https://doi.org/10.1016/B978-0-12-803581-8.10245-0.
[76] S.K. Hubadillah, M.H.D. Othman, T. Matsuura, A.F. Ismail, M.A. Rahman, Z. Harun, J. Jaafar, M. Nomura, Fabrications and applications of low cost ceramic membrane from kaolin: a comprehensive review, Ceram. Int. 44 (2018) 4538–4560, https://doi.org/10.1016/j.ceramint.2017.12.215.
[77] A. Mebrek, Sinterability properties of a ceramic synthesized from Algerian kaolin and spent magnesia-carbon refractory bricks, Int. J. Adv. Manuf. Technol. 117 (2021) 823–834, https://doi.org/10.1007/s00170-021-07637-8.
[78] A. Harabi, F. Zenikheri, B. Boudaira, F. Bouzerara, A. Guechi, L. Foughali, A new and economic approach to fabricate resistant porous membrane supports using kaolin and $CaCO_3$, J. Eur. Ceram. Soc. 34 (2014) 1329–1340, https://doi.org/10.1016/j.jeurceramsoc.2013.11.007.
[79] A. Agarwalla, K. Mohanty, Fabrication and characterization of low-cost kaolin based tubular ceramic membrane for microalgal harvesting, J. Environ. Chem. Eng. 12 (2024) 112089, https://doi.org/10.1016/j.jece.2024.112089.
[80] D. Bouras, M. Fellah, R. Barillé, M. Zerouali, N. Hambli, G.A. El-Hiti, Comparative study of zirconium-zinc oxide thin films on ceramic and glass substrates: structural, optical, and photocatalytic properties, Inorg. Chem. Commun. 171 (2025) 113561, https://doi.org/10.1016/j.inoche.2024.113561.
[81] T. Yokoi, M. Kamitakahara, M. Kawashita, C. Ohtsuki, Formation of organically modified octacalcium phosphate in solutions containing various amounts of benzenedicarboxylic acids, J. Ceram. Soc. Japan 121 (2013) 219–225, https://doi.org/10.2109/jcersj2.121.219.
[82] T.A. Olcoski, A.L. Chinelatto, A.S.A. Chinelatto, Effect of MgO addition on the sinterability and mechanical properties of mullite ceramics, Cerâmica 67 (2021) 261–268, https://doi.org/10.1590/0366-69132021673833075.

[83] D. Chaudhary, S. Singh, V.D. Vankar, N. Khare, ZnO nanoparticles decorated multi-walled carbon nanotubes for enhanced photocatalytic and photoelectrochemical water splitting, J. Photochem. Photobiol. Chem. 351 (2018) 154–161, https://doi.org/10.1016/j.jphotochem.2017.10.018.
[84] D. Bouras, M. Fellah, R. Barillé, A. Iqbal, H. Fouzia, A. Obrosov, G.A. El-Hiti, Thin layers of Fe-doped ZnO deposited by spin-coating for electrolysis and photodetector applications, Trans. Nonferrous Metals Soc. China 35 (2025) 1262–1280, https://doi.org/10.1016/S1003-6326(24)66747-6.
[85] M. D Bouras, D.Z. Fellah, Mohammed, R. Barille, A. Obrosov, G.A. El-Hiti, L. Khezami, Enhanced CO2 sensing properties of Fe/Al-Doped SnO2 thin films: a comprehensive study of structural, optical, and electrical characteristics, J. Alloys Compd. 1034 (2025) 181387, https://doi.org/10.1016/j.jallcom.2025.181387.
[86] F. Aziz, A.B. Gulshan, Z. Usman, M. Rehman, Q. Khalid, M.N. Khan, M. Rafique, Facile eco-friendly synthesis of magnesium oxide nanocarriers using Bauhinia variegata for biomedical and photocatalytic applications, Results Chem. 15 (2025) 102248, https://doi.org/10.1016/j.rechem.2025.102248.
[87] M. Kolli, M. Hamidouche, G. Fantozzi, J. Chevalier, Elaboration and characterization of a refractory based on Algerian kaolin, Ceram. Int. 33 (2007) 1435–1443, https://doi.org/10.1016/j.ceramint.2006.06.009.
[88] B. Boudaira, A. Harabi, F. Bouzerara, F. Zenikheri, L. Foughali, A. Guechi, Preparation and characterization of membrane supports for microfiltration and ultrafiltration using kaolin (DD2) and CaCO3, Desalination Water Treat. 57 (2016) 5258–5265, https://doi.org/10.1080/19443994.2015.1021994.
[89] D. Bouras, M. Fellah, M. Mokrani, R. Barille, H.S. Scott, A. Guesmi, L. Khezami, Structural and antibacterial behaviors of tin dioxide thin films on copper substrates, J. Sci. Adv. Mater. Devices (2025) 100943, https://doi.org/10.1016/j.jsamd.2025.100943.
[90] S. Wells, C.V. Ramana, Effect of hafnium-incorporation on the microstructure and dielectric properties of cobalt ferrite ceramics, Ceram. Int. 39 (2013) 9549–9556, https://doi.org/10.1016/j.ceramint.2013.05.073.
[91] E. Özkol, J. Ebert, R. Telle, An experimental analysis of the influence of the ink properties on the drop formation for direct thermal inkjet printing of high solid content aqueous 3Y-TZP suspensions, J. Eur. Ceram. Soc. 30 (2010) 1669–1678, https://doi.org/10.1016/j.jeurceramsoc.2010.01.004.
[92] M. Yang, N. Lei, J. Liu, L. Yang, B. Li, X. He, Removal of heavy metal ions from wastewater by combined modified kaolin, Desalination Water Treat. 103 (2018) 152–162, https://doi.org/10.5004/DWT.2018.21894.
[93] Z. Hou, B. Cui, L. Liu, Q. Liu, Effect of the different additives on the fabrication of porous kaolin-based mullite ceramics, Ceram. Int. 42 (2016) 17254–17258, https://doi.org/10.1016/J.CERAMINT.2016.08.020.
[94] H. Wang, C. Li, Z. Peng, S. Zhang, Characterization and thermal behavior of kaolin, J. Therm. Anal. Calorim. 105 (2011) 157–160, https://doi.org/10.1007/S10973-011-1385-0.
[95] X. Lao, X. Xu, W. Jiang, J. Liang, J. Liu, Effect of excess MgO on microstructure and thermal properties of cordierite ceramics for high-temperature thermal storage, Ceram. Int. 45 (2019) 22264–22272, https://doi.org/10.1016/J.CERAMINT.2019.07.252.
[96] R.B. Rotti, D.V. Sunitha, R. Manjunath, A. Roy, S.B. Mayegowda, A. P. Gnanaprakash, E.B. Khidir, Green synthesis of MgO nanoparticles and its antibacterial properties, Front. Chem. 11 (2023) 1143614, https://doi.org/10.3389/fchem.2023.1143614.
[97] A. Muhaymin, H.E.A. Mohamed, K. Hkiri, A. Safdar, S. Azizi, M. Maaza, Green synthesis of magnesium oxide nanoparticles using Hyphaenethebaica extract and their photocatalytic activities, Sci. Rep. 14 (1) (2024) 20135, https://doi.org/10.1038/s41598-024-71149-0.
[98] M. Shkir, T.H. AlAbdulaal, M.A. Manthrammel, F.S. Khan, Novel MgO and Ag/MgO nanoparticles green-synthesis for antibacterial and photocatalytic applications: a kinetics-mechanism & recyclability, J. Photochem. Photobiol., A: Chem 449 (2024) 115398, https://doi.org/10.1016/j.jphotochem.2023.115398.
[99] M. RamezaniFarani, M. Farsadrooh, I. Zare, A. Gholami, O. Akhavan, Green synthesis of magnesium oxide nanoparticles and nanocomposites for photocatalytic antimicrobial, antibiofilm and antifungal applications, Catalysts 13 (4) (2023) 642, https://doi.org/10.3390/catal13040642.